UNIVERSITY OF BIRMINGHAM

Research at Birmingham

One-Pot Synthesis of Dealloyed AuNi Nanodendrite as a Bifunctional Electrocatalyst for Oxygen Reduction and Borohydride Oxidation Reaction

Wang, Jiali; Chen, Fuyi; Jin, Yachao; Lei, Yimin; Johnston, Roy

Document Version
Peer reviewed version

Link to publication on Research at Birmingham portal

WILEY-VCH

One-pot Synthesis of Dealloyed AuNi Nanodendrite as a Bifunctional Electrocatalyst for Oxygen Reduction and Borohydride Oxidation Reaction

Jiali Wang,[a] Fuyi Chen,*[a] Yachao Jin,[a] Yimin Lei,[b] and Roy L. Johnston*[c]

Dr. J. Wang, Prof. F. Chen, Dr. Y. Jin
State Key Laboratory of Solidification Processing, Northwestern Polytechnical University,
Xi'an, 710072, China
E-mail: fuyichen@nwpu.edu.cn (Fuyi Chen)

Dr. Y. Lei
School of Advanced Materials and Nanotechnology, Xidian University,
Xi'an, 710126, China

Prof. R. L. Johnston
School of Chemistry, University of Birmingham,
B15 2TT, UK
E-mail: r.l.johnston@bham.ac.uk

A novel one-pot approach for synthesizing the dealloyed nanomaterials at room temperature is introduced for the first time. Such synthetic strategy by applying modulated potentials effectively simplifies the traditional dealloying route which usually requires additional corrosion process to dissolve non-precious metals. The dealloyed AuNi nanodendrites (AuNi NDs) with tunable composition and uniformly elemental distribution are well developed by the one-pot strategy. Impressively, the as-synthesized AuNi NDs exhibit the higher electrochemically active area and definite improvements in electrocatalytic activity for oxygen reduction reaction (ORR) and borohydride oxidation reaction (BOR) than the commercial Pt/C. In particular, the AuNi NDs show 81 mV more positive in half-wave potential and about 3.1 times higher in specific activity (at 0.85 V) for the ORR than Pt/C, together with excellent stability and methanol tolerance, and their superior BOR activity is highly promising among the previously reported catalysts. The unique nanodendritic structure with Au-rich surface and bimetallic electronic effect are the main factors to greatly enhance

1

the bifunctional catalytic performance for the AuNi NDs. Furthermore, such newly-developed facile method is of great significance since it is one of the first examples to effectively engineer dealloyed bimetallic nanostructures via the practical and low-cost route for electrocatalytic applications.

1. Introduction

The increasingly environmental and economic concerns have made clean power sources more attractive.[1] Metal-air batteries and fuel cells provide a promising pathway for alternative energy storage and conversion.[2] However, the electrochemical processes involved in these renewable energy technologies, such as the anodic oxidation reaction and the cathodic reduction reaction, usually suffer from the sluggish kinetics, which greatly reduces the energy efficiency and hinders the further development of such technologies.[3] Therefore, rational design of an electrocatalyst with high activity and long-term durability to effectively accelerate the electrochemical processes is critical and urgent. It has long been thought that the bimetallic nanostructures possess special physicochemical properties compared to their corresponding monometallic counterparts,[4] exhibiting the wide range of potential applications in biosensing,[4a, 4b] optical and magnetic materials,[4b, 4c] drug delivery systems,[4b] and especially in catalysis.[4b, 4d-f] Recently, alloying Pt-group metal (PGM) with other non-noble metals (i.e., Fe, Co, Ni and Cu) has been recognized as a commonly adopted strategy to achieve high-performance electrocatalysts,[5] which would not only significantly improve the catalytic activities of the bimetallic alloys through geometric, ligand and ensemble effects, but effectively decrease the overall cost of the electrocatalyst as a result of the enhanced PGM utilization. However, the non-noble metals in the PGM-based bimetallic nanomaterials are prone to dissolve during the electrochemical process, leading to the severe degradation of the catalytic performance of those catalysts.[6] Thus, to address this problem, the dealloying method, selectively dissolving less-noble metals and rearranging the remaining

atoms by corrosion process, is usually employed as a subsequent and powerful approach for tuning the surface morphology and structure of the bimetallic electrocatalysts to further improve the catalytic activity and stability.[5b, 7] For example, Li et al. reported that the jagged Pt nanowires through dealloying the solution-synthesized PtNi alloy exhibited an ECSA of 118 m^2/g_{Pt} and a specific activity of 11.5 mA/cm^2 (at 0.9 V vs. RHE) for the ORR, delivering a mass activity of 13.6 A/mg_{Pt}, which is around 50 times higher than the commercial state-of-the-art Pt/C.[8] Wang et al. researched the different atomic-level morphology of Cu_3Pt nanoparticles by using chemical and electrochemical dealloying methods, they found that both dealloying processes yielded improved activity and stability towards ORR in comparison with the commercial Pt/C.[9] An atmosphere-controlled chemical dealloying approach was also used by the Strasser group to achieve nanoporous $PtNi_3$ nanoparticles, the resulted $PtNi_3$ catalyst exhibited around 10 and 5 times enhancement in specific and mass activity over the Pt catalyst, respectively.[10]

In general, the traditional method to prepare the dealloyed nanomaterials is a combination of alloying and additional dealloying process.[8-10] Although the combined strategy has been widely used to obtain more efficient electrocatalysts, there are still some limitations that need to be improved: (1) The combined method is always complicated because the subsequent dealloying process requires additional step to etch non-noble metals, which greatly increases time and cost during the catalyst preparation. It is also criticized that, in most previous reports, dealloying process is usually carried out in the strongly corrosive acids or bases,[11] inevitably impacting the overall properties of catalysts to some extent. (2) The alloying approaches reported rely heavily on the organometallic chemistry and extremely long and prudent operations, which is unfriendly and uneconomic for practical applications. In particular, the poisoning effect of organic surfactant on the sample surface adversely affects the performance of electrocatalysts. Therefore, the exploration of a facile, effective and organic-free method

for the controllable synthesis of "clean" dealloyed nanostructures and for the application in the high-performance electrocatalysis is highly essential and technologically important.

Very recently, Au-M (M = Cu, Ni, Co and Zn) bimetallic nanostructures have garnered intensive interest due to their unique catalytic activity and durability in the electrocatalysis.[6, 12] Especially, AuNi nanostructures exhibit a promising prospect in catalyzing a variety of reactions.[6, 12a, 13] Our recent study has indicated that the AuNi dendrites by using electrodeposition and additional dealloying process (labelled as AuNi-DD) showed superior catalytic activity and stability towards ORR compared to the commercial Pt/C.[12a] He et al. prepared the carbon supported AuNi nanoparticles by the chemical method, showing that AuNi/C catalyst apparently promoted the electrode kinetics of BH_4^- oxidation.[13a] Xiao et al. successfully synthesized AuNi nanoparticles on the graphite composite, which exhibited the alloy feature and high activity for hydroquinone.[13b] However, the development of these reported AuNi nanostructures is limited by their single-functional catalytic activity, which are not ready for the current fuel cell application, where Pt-based nanostructures have been developed as the best-performance bifunctional catalysts for both reduction and oxidation reaction.[3a, 14] Moreover, considering that the Nafion membrane in liquid fuel cells has high rate of methanol crossover, engineering bifunctional and anti-poisoning Au-based catalysts is extremely important as a possible replacement for the Pt-based catalysts, which are suffering from the insufficient performance, high cost and low reserves.

Herein, for the first time, we propose a very simple and effective one-pot strategy for directly synthesizing the dealloyed AuNi nanodendrites (AuNi NDs) on the glassy carbon electrode by applying modulated potentials in the same electrolyte solution. The one-pot alloying and dealloying process is strictly controlled by the periodic three-potential-step program (**Scheme 1**). In a typical synthesis, the applied potential was firstly stepped from a higher initial value, where neither Au and Ni deposition happened, then to a lower potential to establish the Au deposition, the potential was finally stepped to a certain value to induce Ni

atoms deposition in parallel with Au deposition (see Experimental Section for details). Most importantly, the potentiostatic stay at the second step was well designed to realize the selective etching effect because the applied potential was much more positive than the standard oxidation potential of Ni but negative than that of Au. As a sharp contrast with other methods, electrodeposition offers the advantages of being relatively environmental friendliness, high deposition rate and easily controlled composition.[12a, 13b] Furthermore, electrochemical alloying and dealloying processes in a single electrolyte solution makes it facile and time-saving to achieve desirable nanostructures at room temperature. It is also of great significance since such novel strategy circumvents the use of corrosive chemicals and organic surfactants. The as-synthesized AuNi NDs exhibit higher bifunctional electrocatalytic performance towards ORR and BOR compared to the commercial Pt/C in alkaline media, moreover, the AuNi catalyst fabricated by the one-pot approach shows a pronounced improvement in the ORR activity than that by using electrodeposition and subsequent dealloying process.[6, 12a] To the best of author's knowledge, such facile and green one-pot synthesis has not been reported hitherto. It is believed that this novel strategy provides new guidelines for optimizing nanostructures synthesis, which would be of great importance in investigating their promising activities in catalysis.

2. Results and Discussion

The dealloyed AuNi NDs catalyst synthesized via the facile one-pot approach was fully characterized by the electron microscopy. As shown in **Figure 1**a, the SEM image shows that the as-synthesized AuNi catalyst consists of uniform nanodendrites with a high morphological yield. The representative bright field TEM image (Figure 1b) further exhibits that each nanodendrite is of highly porous nanostructure with side branches slitting from the trunk, which leads to more accessible active sites for reactants. Compared to the identically synthesized pure Au (Figure S1), the morphology of AuNi catalyst transforms from the

nanoparticles to hierarchical nanodendrites after alloying Au with the transient metal Ni, indicating that the incorporation of Ni atoms by the one-pot electrochemical method facilitates the formation of porous nanodendrites. As revealed by the EDX analysis in Figure S2a, the local Ni/Au atomic ratio of the AuNi NDs is about 0.06 (5.63/94.37), much lower than the initial Ni/Au precursor ratio of 2 (30/15). It is rationally attributed to that the reduction potential of Ni(II) (Ni^{2+}/Ni, -0.257 V vs. SHE (standard hydrogen electrode)) is greatly lower than that of Au(III) (Au^{3+}/Au, +1.50 V vs. SHE), thus Au^{3+} is easier to be reduced compared to Ni^{2+}. Most importantly, the potentiostatic stay at higher potential (+0.8 V vs. SCE for 5 s) of each period during the continuous potential-step process leads to the selective leaching of Ni atoms from the surface of AuNi NDs, consequently resulting in the great decrease of Ni content. The elemental compositions of AuNi catalysts synthesized by the one-pot and traditional combined methods were compared in **Table 1** and Figure S2, the comparable amounts of Ni remain in both AuNi NDs and AuNi-DD catalysts highlight that the one-pot strategy indeed achieves the dealloying effect in a milder way in comparison with the traditional combined method. HRTEM image (Figure 1c) and corresponding Fast Fourier Transform (FFT) patterns (insets in Figure 1c) indicate that AuNi NDs are polycrystalline structure with well-defined lattice planes. The measured lattice spacings of 0.235 and 0.203 nm correspond to the (111) planes of pure metallic Au and Ni. The typical selected area electron diffraction (SAED) pattern (Figure 1d) from the thin tip of a branch shows two sets of Bragg reflections of (111), (220), (222), (300) and (111), (200) for the face centered cubic (fcc) structured Au and Ni, respectively.

To further investigate the elemental distribution and mircostructure of the as-synthesized AuNi NDs, EDX elemental mapping, line scanning and XRD pattern were carried out. Figure 1e and 1f show the elemental mapping for the individual elements, it can be seen that the AuNi NDs are composed of element Au and Ni, demonstrating their bimetallic nature. Based on the location and intensity, both Au and Ni are homogeneously distributed throughout a

single nanodendrite, and only a tiny amount of element Ni remains in the nanodendrite after the one-pot alloying and dealloying process. According to the line profiles along two typical lines (line 1 and 2 in Figure 1e), the AuNi NDs surface shows a much higher intensity for Au atoms, confirming the presence of Au-enriched surface for the electrocatalytic reactions (Figure 1g and 1h). In addition, the elemental mapping and line scanning for the AuNi NDs synthesized at -1.0 V vs. SCE in the last step also exhibit the uniformly elemental distribution, but the nanodendritic surface changes to the Ni-rich surface (Figure S3). The Ni content in the AuNi NDs remarkably increases with the applied potentials going more negative (Table S1 and Figure S4), which is further promoted by the underpotential deposition of Ni atoms for the preformed Au used as the nucleic centers.[15] Meanwhile, as shown in Figure S4, it can be noted that a great morphological variation from aggregated nanoparticles to thick dendrites are observed with fluctuating the applied potential, which indicates that the amount of Ni plays a crucial role in affecting the morphology. The dendritic structures usually provide rapid charge transfer and expose more Au active sites, further improving the catalytic activity for the material. Therefore, to achieve the ideal electrocatalytic activity, the Ni content should be precisely controlled by the applied potentials. In general, homogeneous AuNi nanodendrites with tunable compositions can be easily obtained by applying various potentials in the last step during the one-pot synthesis. The XRD patterns obtained for AuNi NDs and pure Au samples were shown in **Figure 2**, the diffraction peaks of pure Au sample at 2θ values of 38.25°, 44.46°, 64.65°, 77.62°, and 81.76° are attributed to the (111), (200), (220), (311), and (222) planes, respectively, which matches well with those of Au fcc crystal structures (#65-2870). For the AuNi NDs, peaks observed at 44.50° and 51.68° are corresponded to (111) and (200) planes of Ni (#65-0380), the XRD pattern of AuNi NDs contains high intensity diffraction peaks of the individual metallic Au and Ni that would indicate the formation of AuNi bimetal. In comparison with the peaks of pure Au, it is noteworthy that the Au (111) diffraction peak of the AuNi NDs is slightly shifted to higher 2θ angles (Figure S5). Based on

the Bragg equation, the interplanar spacing of Au (111) planes in the AuNi NDs is calculated

to be 0.2347 nm, which demonstrates a neglectable 0.17 % lattice compression compared to

that of pure Au (0.2351 nm), further identifying that the as-synthesized AuNi nanodendritic

structure is mainly mixed metal nature including fcc structured Au and Ni.

As to the in-deep origin of enhanced catalytic activity of the as-synthesized AuNi NDs,

the surface species and electronic structures were studied by the XPS measurement. Through

comparing the survey spectra of AuNi NDs and pure Au catalysts (**Figure 3**a), clear peaks

belong to Au and Ni were observed for the AuNi NDs, confirming the formation of bimetallic

AuNi nanostructures. According to the XPS composition analysis (Table 1), the Ni content in

the AuNi NDs is only 5.71 at %, which is consistent with the result of EDX measurement and

further confirms the uniform distributions of Au and Ni in both bulk and the dendritic surface.

In the deconvoluted XPS spectrum of Ni 2p (Figure 3b), two peaks located at 852.9 and 870.2

eV are assigned to the binding energies of Ni $2p_{3/2}$ and Ni $2p_{1/2}$, which indicates the presence

of metallic Ni at or close to the electrode surface. Additionally, two peaks centered at 855.6

and 873.3 eV are attributed to the main peaks of oxidized $Ni^{2+/3+}$ $2p_{3/2}$ and $Ni^{2+/3+}$ $2p_{1/2}$,

respectively, since the Ni atoms are susceptible to oxidation, and other two peaks located at

861.5 and 880.3 eV correspond to the satellite peaks of the oxidized $Ni^{2+/3+}$.[16] Figure 3c

shows the Au 4f core-level (CL) spectrum of the pure Au catalyst, a doublet with the binding

energies located at 87.67 and 84.07 eV are assigned to Au $4f_{5/2}$ and Au $4f_{7/2}$, respectively,

corresponding to the zero valent Au^0. Compared to the pure Au, the Au 4f binding energies of

AuNi NDs exhibit a clear shift to the lower values (87.57 and 83.97 eV attributed to the Au

$4f_{5/2}$ and Au $4f_{7/2}$, respectively). As generally agreed, the d-band character of Au dominates

the band structures of the catalyst surface and then affects the electrocatalytic activity towards

ORR.[17] It has been recently proved that the Au 4f CL shifting to the lower binding energies

indicated the upshift of the d-band center with respect to the Fermi level,[12a] leading to the

stronger adsorption energy between Au and O, and thus higher ORR catalytic activity. Figure

3d presents the valence band spectra (VBS) of AuNi NDs and pure Au catalysts, the d-band center of the AuNi NDs (dark grey line) is closer to the Fermi level than that of pure Au (orange line), further demonstrating that the modification of the electronic structure appears after the one-pot alloying and dealloying process. The resulted d-band center upshift for the AuNi NDs may alter the chemisorption of reactants, intermediates and products and thus enhance the ORR electrochemical performance.[18]

The hierarchical AuNi NDs were investigated for their ORR and BOR performance to demonstrate the superior bifunctional catalytic activities. As shown in **Figure 4**a, the ORR performance of AuNi NDs, AuNi-DD, pure Au and commercial Pt/C catalysts were studied by the linear sweep voltammetry (LSV) curves in O_2-saturated 0.1 M KOH solution at the rotation rate of 1600 rpm. The LSV curve of AuNi NDs exhibits two distinguishable potential regions: the mixed kinetic-diffusion control region between 0.8 and 1.1 V and the diffusion controlled region below 0.8 V. In the kinetic-diffusion region, it can be seen that AuNi NDs catalyst via the one-pot strategy exhibits much higher half-wave potential ($E_{1/2}$) at 0.911 V, which is 81 and 121 mV more positive than that of the commercial state-of-the-art Pt/C (0.830 V) and pure Au (0.790 V), respectively. Intriguingly, the as-synthesized AuNi NDs catalyst even shows a 15 mV positive shift relative to the recently reported AuNi-DD catalyst (0.896 V),[12a] indicating that the dramatically improved catalytic activity towards ORR at lower overpotentials can be more easily obtained by using the effective one-pot route than the traditional combined approach. In addition, AuNi NDs also exhibit more positive onset potential (E_{onset}) than the Pt/C, and both the AuNi NDs and commercial Pt/C have the comparable diffusion-limiting current density of ~5.0 mA cm^{-2} (**Table 2**). Figure S6 presents LSV curves of the AuNi NDs synthesized under different potential values in the last step, -0.8 V vs. SCE is demonstrated to be the optimized potential value for the ORR catalysis. The more negative the applied voltage value is, the more Ni atoms remain in the nanodendrites. This result indicates that the efficient electrocatalytic oxygen reduction could be realized by

9

introducing an appropriate amount of Ni atoms into Au, which can be strongly supported by the XPS measurement (Figure S7). To gain more insights into the reaction kinetics for the ORR, the mass transport corrected Tafel plots were shown in Figure 4b. The plots depict that the AuNi NDs catalyst shows enhanced ORR activity than the commercial Pt/C catalyst. For instance, the kinetic current density of AuNi NDs at 0.90 V is apparently higher than that of commercial Pt/C. Moreover, the AuNi NDs catalyst has a Tafel slope of 48.1 mV dec^{-1} compared to 71.5 mV dec^{-1} calculated for the Pt/C catalyst. It is widely accepted that the Tafel slope is an indication of the mechanism of surface reaction on the electrode, related to the variation of adsorbed oxygenated species nature and their coverage corresponding to the potential.[19] The lower Tafel slope of the AuNi NDs indicates that their more excellent catalytic activity towards ORR than the commercial Pt/C, due to the facile oxygen adsorption and subsequent reduction reaction.

We used the cyclic voltammetry (CV) curves to evaluate the electrochemically active surface areas (ECSAs) of different electrocatalysts. Figure 4c shows the voltammetric behaviors of AuNi NDs and pure Au catalysts in 0.5 M N_2-saturated H_2SO_4 solution along with that of the commercial Pt/C (inset in Figure 4c) for comparison. The AuNi NDs display a higher ECSA of 11.0 cm^2, about 4 times higher than that of pure Au catalyst (2.8 cm^2), which substantiates the apparent structural advantage of AuNi NDs over the pure Au to obtain more accessible active sites (i.e., kink or step sites) for the oxygen reduction. In order to compare the ORR intrinsic efficacy of different catalysts, we also further calculated the specific activity (SA), in which the kinetic currents were normalized with respect to the ECSA. Figure 4d shows the specific activities of AuNi NDs and the commercial Pt/C catalyst at different potentials, their specific activities are 0.46 and 0.15 mA cm^{-2} at 0.85 V for AuNi NDs and the commercial Pt/C, respectively. At 0.9 V, the corresponding values are 0.11 and 0.06 mA cm^{-2}. In particular, the specific activity of AuNi NDs is about 3.1 times higher than that of the commercial state-of-the-art Pt/C catalyst at 0.85 V. Meanwhile, the mass activity of AuNi

10

NDs (0.090 A mg^{-1}$_{Au}$) is comparable to that of the commercial Pt/C (0.091 A mg^{-1}$_{Pt}$) (Figure S8). As compared to the previously reported AuNi alloys and other dealloyed bimetallic electrocatalyst (Table S2), the as-synthesized AuNi NDs catalyst also exhibits more significant enhancement in electrocatalytic activity towards ORR. Figure 4e provides the rotation-rate-dependent current-potential curves of AuNi NDs (similar curves for the commercial Pt/C and pure Au are given in Figure S9). The limiting current density increases with an increase in the rotation speed, which suggests that the catalytic reaction of the AuNi NDs towards ORR is controlled by the oxygen diffusion. To investigate the ORR pathway, the electron transfer number (n) was calculated to be ~ 3.9 from the slopes of the Koutecky-Levich plots (inset in Figure 4e), indicating a dominant four-electron pathway towards ORR and the nearly complete reduction of O_2 to OH^- on the surface of the modified electrode, similar to the ORR process catalyzed by the commercial Pt/C catalyst (Figure 4f).

The catalytic stability of AuNi NDs towards ORR was further evaluated through the chronoamperometric (CA) measurement at 0.82 V for 10 h in O_2-saturated 0.1 M KOH aqueous solution at 1600 rpm (**Figure 5**a). During the period, about 90 % of the original current density is retained for AuNi NDs, whereas the commercial Pt/C shows much higher current loss of 39 %, clearly confirming the AuNi NDs catalyst possesses the superior long-term stability compared to the commercial Pt/C. The structural evolution and compositional characteristics of AuNi NDs after the long-term stability test were investigated by the TEM. As shown in Figure S10, the AuNi NDs catalyst still remains the hierarchical dendritic morphology, uniformly elemental distribution, and comparable Ni content relative to the initial AuNi NDs after the stability test. Thus, it can be concluded that such good stability of AuNi NDs might be related to the stable nanodendritic structure with Au-enriched surface, since the element Au has recently been reported to impart kinetic stabilization in electrocatalysis of the binary/ternary system.[20] Additionally, the support-free AuNi catalyst avoiding the carbon corrosion associated with Pt/C nanoparticles also makes contributions to

11

such better stability. The methanol tolerance during the ORR process is a necessary characteristic for the cathode catalyst in terms of the fuel cell's power efficiency,[21] the crossover effect was measured by the CA measurement for AuNi NDs and the Pt/C catalysts. As shown in Figure 5b, for AuNi NDs, the injection of methanol (1 M) induces much slighter responsive current, while the commercial Pt/C immediately undergoes a drastic decrease after the addition of methanol, which suggests that the AuNi NDs catalyst shows the unique tolerance to methanol during catalyzing the oxygen reduction reaction. Figure 5c and 5d compare the cyclic voltammogram (CV) curves of AuNi NDs and the commercial Pt/C in N_2-saturated 0.1 M KOH solution with and without methanol. A Pt oxide peak emerges at 0.8 V in the solution without methanol for the commercial Pt/C, but in the presence of methanol, a sharp methanol oxidation peak appears. As expected, the commercial Pt/C is catalytically active not only for the ORR but also for the methanol oxidation. As a contrast, there is no methanol oxidation peaks observed in the CV curves of the AuNi NDs, which indicates that the good tolerance towards methanol is a result of the higher selectivity for the ORR than for the methanol oxidation below the potential of 1.2 V observed for the AuNi NDs.[21] Therefore, the AuNi NDs catalyst has the great potential to be a new class of high-performance cathode electrocatalyst for the direct methanol fuel cells.

Furthermore, the electrocatalytic performance of AuNi NDs towards sodium borohydride oxidation reaction (BOR) under the alkaline media was also evaluated, which was compared with the commercial Pt/C and other previously reported BOR electrocatalysts. **Figure 6**a and 6b show the CV curves of AuNi NDs, pure Au and the commercial Pt/C catalysts in N_2-saturated 3 M NaOH aqueous solution containing 0.05 M sodium borohydride at a scan rate of 50 mV s^{-1}. As can be seen from the CV curve for the AuNi NDs (Figure 6a), in the positive potential sweep, a peak attributed to the potentially eight-electron BH_4^- oxidation is observed around 0.70 V, in the reverse potential sweep, the strong peak observed at 1.2 V can be assigned to the absorbed borohydroxides as an intermediate during BOR. The peak current

12

density of AuNi NDs is around 5.7 times higher than that of the pure Au catalyst (91 vs. 16

mA cm^{-2}). The higher current density indicates the improved catalytic activity of the AuNi

NDs for the sodium borohydride oxidation relative to the monometallic Au, which agrees

with the previous report of AuNi/C nanoparticles for the enhanced BOR activity.[13a]

Moreover, we benchmarked such superior BOR catalytic activity with that of the commercial

Pt/C catalyst. As shown in Figure 6b, an oxidation peak between 0.2 and 0.4 V is due to the

oxidation of H_2 generated by the catalytic hydrolysis of BH_4^-, it can be seen that the AuNi

NDs catalyst outperforms the Pt/C catalyst both in the peak current density of BH_4^- oxidation

(91 mA cm^{-2} at 0.7 V vs. 13 mA cm^{-2} at 1.1 V) and the onset potential (0.3 vs. 0.9 V). Most

importantly, the as-synthesized AuNi NDs catalyst is still highly promising among the state-

of-the-art reported BOR electrocatalysts (Table S3), suggesting their great potential as a

bifunctional electrocatalyst. Such enhanced activity towards BOR may come from the

electronic effect between Au and Ni. Additionally, the morphological advantage of AuNi NDs

with a high concentration of terraces and edges also further facilitates the transport of

electrons and then the oxidation of sodium borohydride.

From all the aforementioned results, we can conclude that the novel one-pot synthetic

route could be used to simply achieve the dealloyed AuNi NDs and simultaneously tune the

electronic properties, thus obtaining the excellent electrocatalytic performance towards ORR,

BOR and the anti-poisoning ability to methanol. We also prepared the AuCu electrocatalyst

by the same one-pot synthetic strategy (Figure S11 and S12) and achieved a half-wave

potential of 0.848 V and a specific activity of 0.40 mA cm^{-2} at 0.85 V for the ORR as well as

the enhanced BOR activity, which are also much higher than those of the commercial Pt/C

catalyst (Figure S13 and S14). The relatively lower catalytic activity compared to the AuNi

catalyst is ascribed to the structural variation (nanoparticles vs. nanodendrites) and the

resulted smaller ECSA (3 cm^2 vs. 11 cm^2). These studies further demonstrate the generality

and validity of our novel one-pot approach to derive dealloyed electrocatalyst with developed nanostructures and various promising catalytic properties.

3. Conclusion

In summary, for the first time, we have successfully synthesized hierarchical AuNi NDs based on a novel one-pot synthetic strategy. The one-pot protocol shows that neither Au and Ni deposition happened at the first short stage, then pure Au atoms were deposited at the second stage, finally the co-deposition of Au and Ni atoms under lower potential was responsible for the formation of AuNi hierarchical nanodendrites. Moreover, at the second stage, the applied deposition voltage was set between the standard oxidation potential of Au and Ni, realizing the selective etching of Ni atoms from the preformed AuNi NDs. Impressively, the as-synthesized AuNi NDs catalyst exhibits higher electrochemically active surface area and the enhanced electrocatalytic performance for the ORR and BOR compared to the commercial state-of-the-art Pt/C catalyst in alkaline solution. Additionally, the AuNi NDs catalyst also presents high selectivity for the ORR and superior tolerance to methanol. The higher bifunctional catalytic performance of the AuNi NDs can be ascribed to the unique nanodendritic structure with the Au-rich surface and bimetallic electronic effect. We believe that this novel one-pot strategy for the synthesis of the dealloyed Au-based nanostructures might open a new avenue to the construction of other bi/multi-metallic electrocatalysts with various promising applications.

4. Experimental Section

Chemicals: Hydrogen tetrachloroaurate (III) hydrate ($HAuCl_4 \cdot 4H_2O$), nickel (II) sulfate hexahydrate ($NiSO_4 \cdot 6H_2O$), Sodium borohydride ($NaBH_4$), sodium sulfate (Na_2SO_4), sulfuric acid (H_2SO_4), potassium hydroxide (KOH) and sodium hydroxide (NaOH) were purchased from Tianjin Fuchen Chemical Reagent Co., Ltd. (China). Pt/C catalyst (Pt loading 20 wt %, fuel cell grade) was commercially available from Johnson Matthey Fuel Cells. Ethanol was

purchased from Xi'an Shunda. All chemicals used in the experiment were of reagent grade and used without any further purification. All aqueous solutions were prepared with ultrapure water with the resistance of 18.25 MΩ cm.

One-pot synthesis of the dealloyed AuNi nanodendrites: Glassy carbon rotating disk electrode (RDE, 0.196 cm^2) was successively polished with 0.3 and 0.05 μm alumina slurry and ultrasonically cleaned in acetone and ultrapure water before electrodeposition. The synthesis of AuNi bimetallic catalysts was accomplished in a three-electrode electrochemical cell at room temperature, using the pretreated RDE as the working electrode, and a gold foil and a saturated calomel electrode (SCE) as the counter and reference electrodes, respectively. The AuNi NDs catalyst was synthesized by using the periodic three-potential-step program under the following optimized conditions; the single electrolyte consisted of 0.1 M Na$_2$SO$_4$, 0.015 M HAuCl$_4$ and 0.030 M NiSO$_4$ (molar ratio: Au:Ni = 1:2) with ultrapure water as the solvent. The potentials in each period were controlled by the CHI 660C electrochemical workstation (Shanghai Chenhua Apparatus, China). The applied potential for one typical cycle was firstly stepped from +1.2 V vs. SCE, then to +0.8 V vs. SCE for a duration of 5 s to establish the diffusion-limited Au deposition, and finally held at -0.8 V vs. SCE for 20 s to induce the co-deposition of Ni and Au atoms. Moreover, the second step of each cycle was deliberately designed to etching Ni atoms from the preformed AuNi nanostructure. After 35 cycles, the modified RDE was carefully washed by ethanol and ultrapure water for several times and allowed to dry naturally in air. The loading amount of Au was determined to be 0.286 mg cm^{-2} for the AuNi NDs by calculating electron transfer numbers according to the Coulomb quantity during the electrodeposition process. The same procedure was used to synthesize different AuNi electrocatalysts by simply adjusting the applied potentials (i.e., the potential value in the last step). For comparison, pure Au modified glassy carbon disk electrode was prepared under identical experimental conditions by using the electrolyte without NiSO$_4$. Additionally, the AuNi catalyst synthesized by the traditional combined method reported in

our previous work,[12a] namely, electrochemical deposition and subsequent dealloying process, was also prepared for comparison, which was labelled as AuNi-DD for simplicity.

Physical characterization: The morphology and structure of the as-prepared nanostructures were observed by the high-resolution transmission electron microscopy (HRTEM, FEI Tecnai F30), and the elemental compositions were recorded with energy dispersive X-ray (EDX) spectroscopy. Scanning electron microscopy (SEM) was conducted with a FEI NovaSEM 450 field emission scanning electron microscope. The phase and crystallinity of the samples were characterized using the X-ray diffraction (XRD) spectroscope by the PANalytical X'Pert Pro MPD with Cu Kα radiation (λ = 1.5406 Å). The accelerating voltage and current employed were 40 KV and 40 mA, respectively. X-ray photoelectron spectroscopy (XPS) characterization was performed on an ESCALAB 250 instrument under ultrahigh vacuum (10^{-9} Torr) using monochromated Al Kα radiation (hν = 1486.6 eV) to examine the surface component and electronic structure, all the binding energy were calibrated by the carbon peak (C 1s) at about 284.5 eV.

Electrochemical characterization: The ORR experiments were conducted in a conventional three-electrode system assembled with the catalyst deposited RDE as the working electrode, platinum wire as the counter electrode and mercury-mercury oxide (MMO) Hg│HgO│(NaOH 1M) as the reference electrode. All potential values in this paper were referred to the reversible hydrogen electrode (RHE) unless otherwise stated. All electrochemical measurements were carried out at room temperature using research-grade gases. For the ORR activity on a RDE, the linear sweep voltammetry (LSV) was measured at a sweep rate of 10 mV s^{-1} with the different rotation rate (400, 800, 1200, 1600 and 2000 rpm) in O$_2$-saturated 0.1 M KOH solution. The following equations (Koutecky-Levich equation, j^{-1} versus $\omega^{-1/2}$) were used for the calculation of the kinetic current and electron transfer number (n) per oxygen molecule.

$$j^{-1} = j_k^{-1} + j_d^{-1} = j_k^{-1} + (B\omega^{1/2})^{-1} \tag{1}$$

$$B = 0.62\text{n}FC_0D_0^{2/3}\nu^{-1/6} \tag{2}$$

Where j is the actual current density, j_k and j_d are the kinetic- and diffusion-limiting current densities, respectively, B is the Levich slope, ω is the angular velocity of the RDE ($\omega = 2\pi N$, N is the linear rotation speed in rpm), n is the electron transfer number, F is the Faraday constant (96485 C mol^{-1}), C_0 is the bulk concentration of O_2 (1.2×10^{-6} mol cm^{-3}), D_0 denotes the diffusion coefficient of O_2 (1.9×10^{-5} cm^2 s^{-1}) in 0.1 M KOH aqueous solution, and ν represents the kinetic viscosity of the electrolyte (0.01 cm^2 s^{-1}).[22]

The ORR stability and methanol tolerance were recorded by the chronoamperometric (CA) measurement. The methanol tolerance test was performed by introducing methanol into the O_2-saturated 0.1 M KOH solution (1 M methanol) at 3000 s. The electrochemical BOR was conducted by cyclic voltammetry (CV) at the scan rate of 50 mV s^{-1} in N_2-saturated 3 M NaOH solution containing 0.05 M NaBH$_4$. The electrochemically active surface area (ECSA) of AuNi catalyst was determined by measuring the charge collected in the region of Au oxide reduction and assuming the charge density of 390 μC cm^{-2}.[23] The commercial Pt/C catalyst was used as a baseline catalyst, and the Pt/C loading on the RDE was calculated as 0.122 mg cm^{-2}. The ECSA of commercial Pt/C was evaluated by integrating the charge in the hydrogen adsorption/desorption region, assuming a value of 210 μC cm^{-2} for the adsorption of a hydrogen monolayer.[23-24] To ensure the reproducibility of each sample, we fabricated at least three separated samples for each kind of catalyst.

Supporting Information
Supporting Information is available from the Wiley Online Library or from the author.

[1]   a) G. Liu, P. Li, G. Zhao, X. Wang, J. Kong, H. Liu, H. Zhang, K. Chang, X. Meng, T. Kako, *J. Am. Chem. Soc.* **2016**, *138*, 9128; b) J. L. White, M. F. Baruch, J. E. Pander Iii, Y. Hu, I. C. Fortmeyer, J. E. Park, T. Zhang, K. Liao, J. Gu, Y. Yan, *Chem. Rev.* **2015**, *115*, 12888.

[2]   a) Y. Jin, F. Chen, *Electrochim. Acta* **2015**, *158*, 437; b) M. Shao, Q. Chang, J.-P. Dodelet, R. Chenitz, *Chem. Rev.* **2016**, *116*, 3594.

[3]   a) N. Zhang, Y. Feng, X. Zhu, S. Guo, J. Guo, X. Huang, *Adv. Mater.* **2016,** DOI: 10.1002/adma.201603774; b) L. Chen, H. Guo, T. Fujita, A. Hirata, W. Zhang, A. Inoue, M. Chen, *Adv. Funct. Mater.* **2011**, *21*, 4364.

[4]   a) Y. Chen, H. Cao, W. Shi, H. Liu, Y. Huang, *Chem. Commun.* **2013**, *49*, 5013; b) K. D. Gilroy, A. Ruditskiy, H.-C. Peng, D. Qin, Y. Xia, *Chem. Rev.* **2016**, *116*, 10414; c) V. A. Bharathan, G. K. Raj, P. A. Joy, C. P. Vinod, *Particle & Particle Systems Characterization* **2014**, *31*, 236; d) J. L. Fernández, D. A. Walsh, A. J. Bard, *J. Am. Chem. Soc.* **2005**, *127*, 357; e) A. Vysakh, C. L. Babu, C. Vinod, *J. Phys. Chem. C* **2015**, *119*, 8138; f) J. W. Hong, D. Kim, Y. W. Lee, M. Kim, S. W. Kang, S. W. Han, *Angew. Chem.* **2011**, *123*, 9038.

[5]   a) D. Wang, H. L. Xin, R. Hovden, H. Wang, Y. Yu, D. A. Muller, F. J. Disalvo, H. D. Abruña, *Nat. Mater.* **2013**, *12*, 81; b) X. Ge, L. Chen, J. Kang, T. Fujita, A. Hirata, W. Zhang, J. Jiang, M. Chen, *Adv. Funct. Mater.* **2013**, *23*, 4156; c) V. R. Stamenkovic, B. S. Mun, M. Arenz, K. J. Mayrhofer, C. A. Lucas, G. Wang, P. N. Ross, N. M. Markovic, *Nat. Mater.* **2007**, *6*, 241; d) H. Yano, M. Kataoka, H. Yamashita, H. Uchida, M. Watanabe, *Langmuir* **2007**, *23*, 6438.

[6]   M. H. Naveen, N. G. Gurudatt, H. B. Noh, Y. B. Shim, *Adv. Funct. Mater.* **2016**, *26*,

1590.

[7]   J. L. Shui, C. Chen, J. Li, *Adv. Funct. Mater.* **2011**, *21*, 3357.

[8]   M. Li, Z. Zhao, T. Cheng, A. Fortunelli, C.-Y. Chen, R. Yu, Q. Zhang, L. Gu, B. V. Merinov, Z. Lin, *Science* **2016**, *354*, 1414.

[9]   D. Wang, Y. Yu, J. Zhu, S. Liu, D. A. Muller, H. C. D. AbruñA, *Nano Lett.* **2015**, *15*, 1343.

[10]   L. Gan, C. Cui, S. Rudi, P. Strasser, *Top. Catal.* **2014**, *57*, 236.

[11]   a) P. Strasser, S. Kühl, *Nano Energy* **2016**, *29*, 166; b) Y. Song, X. Zhang, S. Yang, X. Wei, Z. Sun, *Fuel* **2016**, *181*, 269.

[12]   a) J. Wang, F. Chen, Y. Jin, R. L. Johnston, *J. Mater. Chem. A* **2016**, *4*, 17828; b) N. Zhang, X. Chen, Y. Lu, L. An, X. Li, D. Xia, Z. Zhang, J. Li, *Small* **2014**, *10*, 2662; c) H.-B. Noh, M. H. Naveen, Y.-J. Choi, E. S. Choe, Y.-B. Shim, *Chem. Commun.* **2015**, *51*, 6659.

[13]   a) P. He, Y. Wang, X. Wang, F. Pei, H. Wang, L. Liu, L. Yi, *J. Power Sources* **2011**, *196*, 1042; b) F. Xiao, L. Yang, F. Zhao, B. Zeng, *Anal. Bioanal. Electrochem.* **2013**, *5*, 154; c) M. G. Hosseini, M. Abdolmaleki, F. Nasirpouri, *Electrochim. Acta* **2013**, *114*, 215; d) Z. Zheng, Y. H. Ng, D. W. Wang, R. Amal, *Adv. Mater.* **2016**, *28*, 9949.

[14]   Z. Zhang, Z. Luo, B. Chen, C. Wei, J. Zhao, J. Chen, X. Zhang, Z. Lai, Z. Fan, C. Tan, *Adv. Mater.* **2016**, *28*, 8712.

[15]   K.-H. Choi, Y. Jang, D. Y. Chung, P. Seo, S. W. Jun, J. E. Lee, M. H. Oh, M. Shokouhimehr, N. Jung, S. J. Yoo, *Chem. Commun.* **2016**, *52*, 597.

[16]   a) C. Chen, Y. Kang, Z. Huo, Z. Zhu, W. Huang, H. L. Xin, J. D. Snyder, D. Li, J. A. Herron, M. Mavrikakis, *Science* **2014**, *343*, 1339; b) H. Ali-LöYtty, M. W. Louie, M. R. Singh, L. Li, H. G. Sanchez Casalongue, H. Ogasawara, E. J. Crumlin, Z. Liu, A. T. Bell, A. Nilsson, *J. Phys. Chem. C* **2016**, *120*, 2247.

[17]   a) G. Wang, L. Xiao, B. Huang, Z. Ren, X. Tang, L. Zhuang, J. Lu, *J. Mater. Chem.*

2012, *22*, 15769; b) F. Lima, J. Zhang, M. Shao, K. Sasaki, M. Vukmirovic, E. Ticianelli, R. Adzic, *J. Phys. Chem. C* **2007**, *111*, 404.

[18]   X. Tan, S. Prabhudev, A. Kohandehghan, D. Karpuzov, G. A. Botton, D. Mitlin, *ACS Catal.* **2015**, *5*, 1513.

[19]   a) V. M. Dhavale, S. Kurungot, *ACS Catal.* **2015**, *5*, 1445; b) S. Knani, L. Chirchi, W. Napporn, S. Baranton, J. Léger, A. Ghorbel, *J. Electroanal. Chem.* **2015**, *738*, 145.

[20]   a) X. Sun, D. Li, Y. Ding, W. Zhu, S. Guo, Z. L. Wang, S. Sun, *J. Am. Chem. Soc.* **2014**, *136*, 5745; b) J. Zhang, K. Sasaki, E. Sutter, R. Adzic, *Science* **2007**, *315*, 220.

[21]   U. Din, M. Aizaz, F. Saleem, B. Ni, Y. Yong, X. Wang, *Adv. Mater.* **2016**, DOI: 10.1002/adma.201604994.

[22]   a) Y. Jin, F. Chen, Y. Lei, X. Wu, *ChemCatChem* **2015**, *7*, 2377; b) X.-R. Li, X.-L. Li, M.-C. Xu, J.-J. Xu, H.-Y. Chen, *J. Mater. Chem. A* **2014**, *2*, 1697.

[23]   S. Trasatti, O. Petrii, *Pure Appl. Chem.* **1991**, *63*, 711.

[24]   B. Lim, M. Jiang, P. H. Camargo, E. C. Cho, J. Tao, X. Lu, Y. Zhu, Y. Xia, *science* **2009**, *324*, 1302.
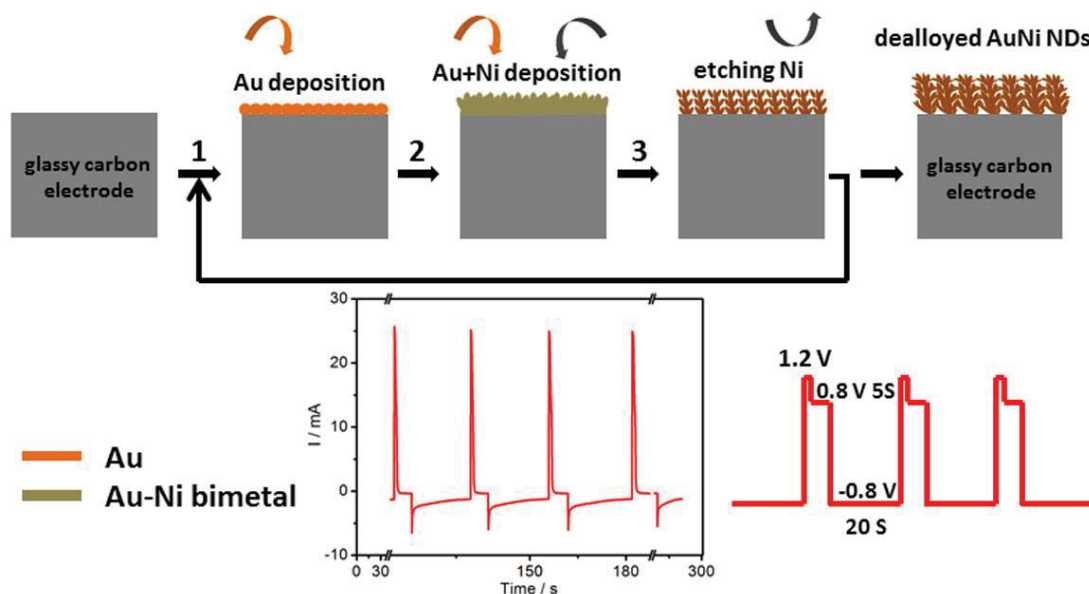
Scheme 1. Schematic illustration of the formation of the hierarchical AuNi nanodendrites by the one-pot synthetic strategy, the alloying and dealloying processes were strictly controlled by the periodic three-potential-step program in the same electrolyte solution. Step 1, electrochemical deposition of Au; Step 2, co-deposition of Au and Ni atoms and formation of the AuNi bimetal; Step 3, etching Ni atoms from the surface of preformed AuNi bimetal and formation of thick nanodendrites; Finally, formation of the hierarchical AuNi nanodendrites with a high level of porosity after multicyclic alloying and dealloying process.
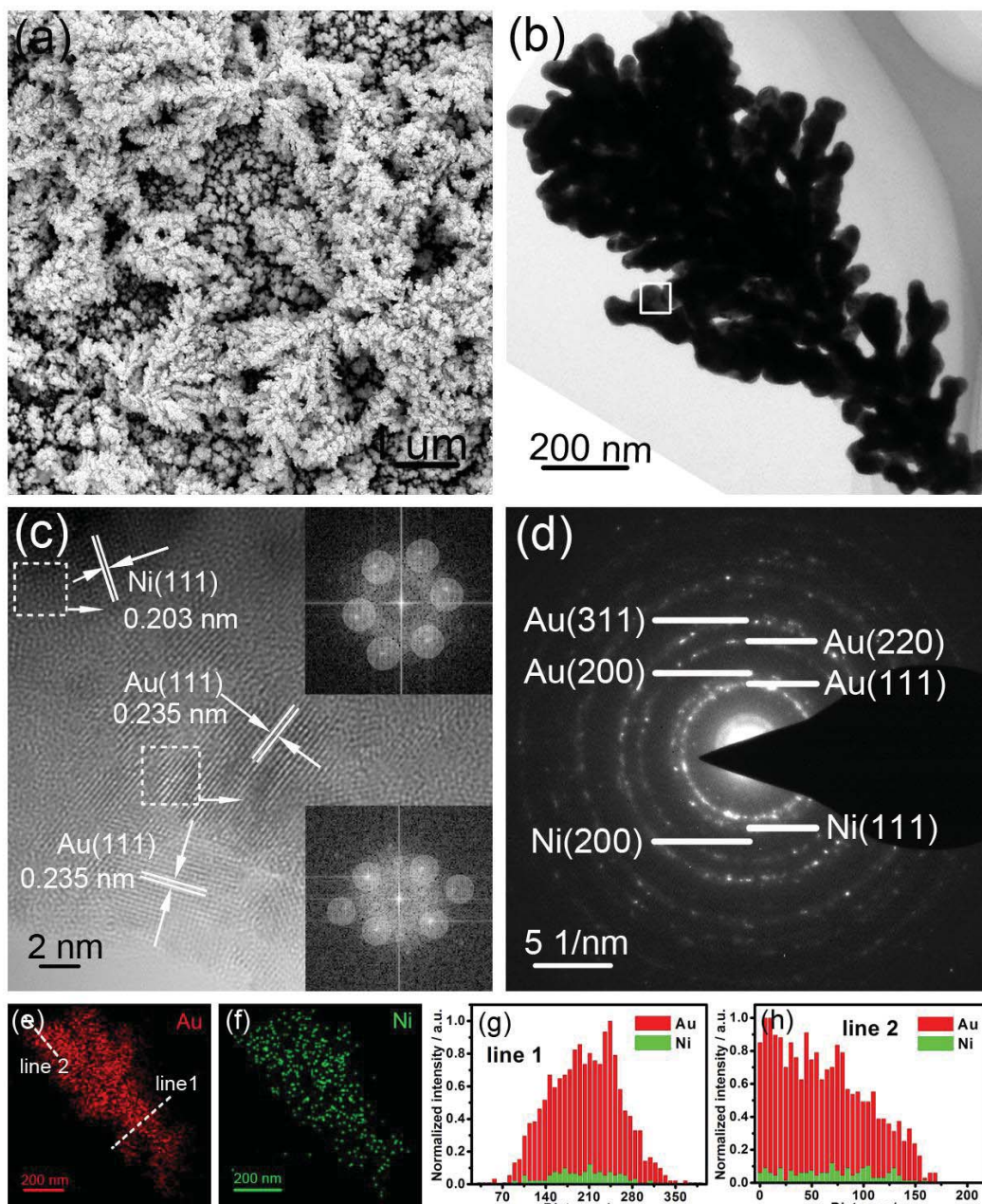
Figure 1. General characterization of the as-synthesized AuNi electrocatalyst. (a) SEM and (b) Bright field TEM images of the AuNi NDs synthesized by the one-pot strategy in the single electrolyte solution. (c) HRTEM image of the AuNi NDs, the insets indicate the corresponding Fast Fourier Transform (FFT) patterns obtained in the framed part (dashed line) in (c). (d) SAED pattern of the AuNi NDs. (e, f) EDX elemental mapping of a single representative nanodendrite. Red represents Au, and green represents Ni. The unique AuNi nanodendrite with uniformly distributed Au and Ni can be found. (g, h) EDX line profiles extracted from two typical lines in (e). Only a trace amount of element Ni remains in the nanodendrite after the one-pot alloying and dealloying process, indicating the formation of AuNi NDs with the Au-rich surface.
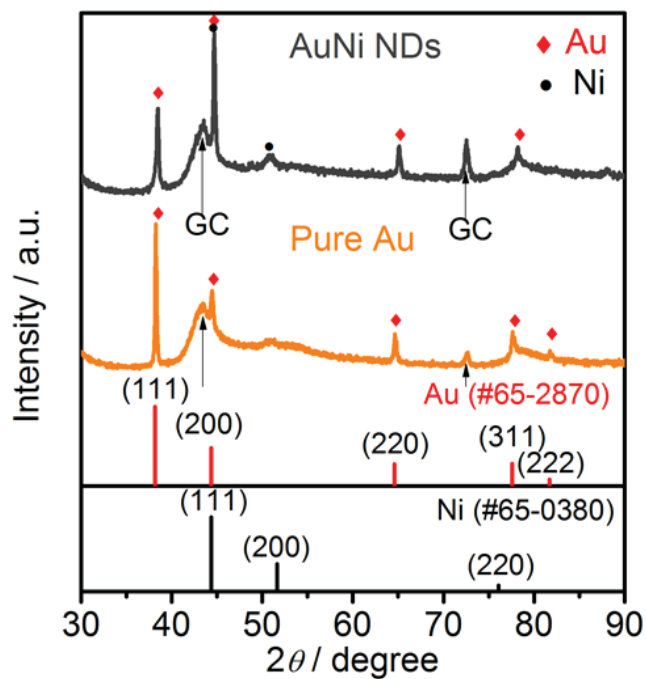
Figure 2. XRD patterns for the AuNi NDs and pure Au samples. Bar diagram: Au #65-2870, Ni #65-0380.
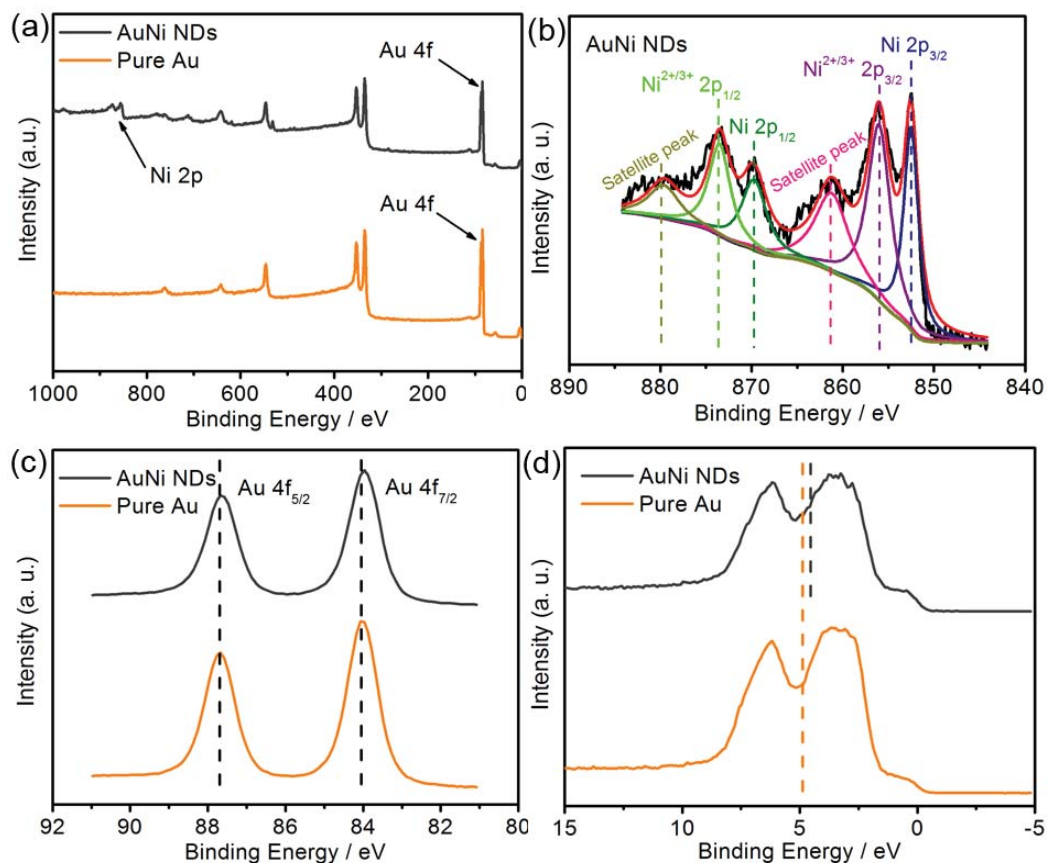
Figure 3. (a) The XPS survey spectra of the as-synthesized AuNi NDs and pure Au. (b) High-resolution spectrum of Ni 2p region for AuNi NDs. (c) High-resolution spectra of Au 4f region for AuNi NDs and pure Au samples, exhibiting that the Au 4f CL of AuNi NDs shifts to the lower binding energies compared to the pure Au sample. (d) Valence band spectra (VBS) for the AuNi NDs (dark grey line) and pure Au (orange line), showing the closer location with respect to the Fermi level for the AuNi NDs.
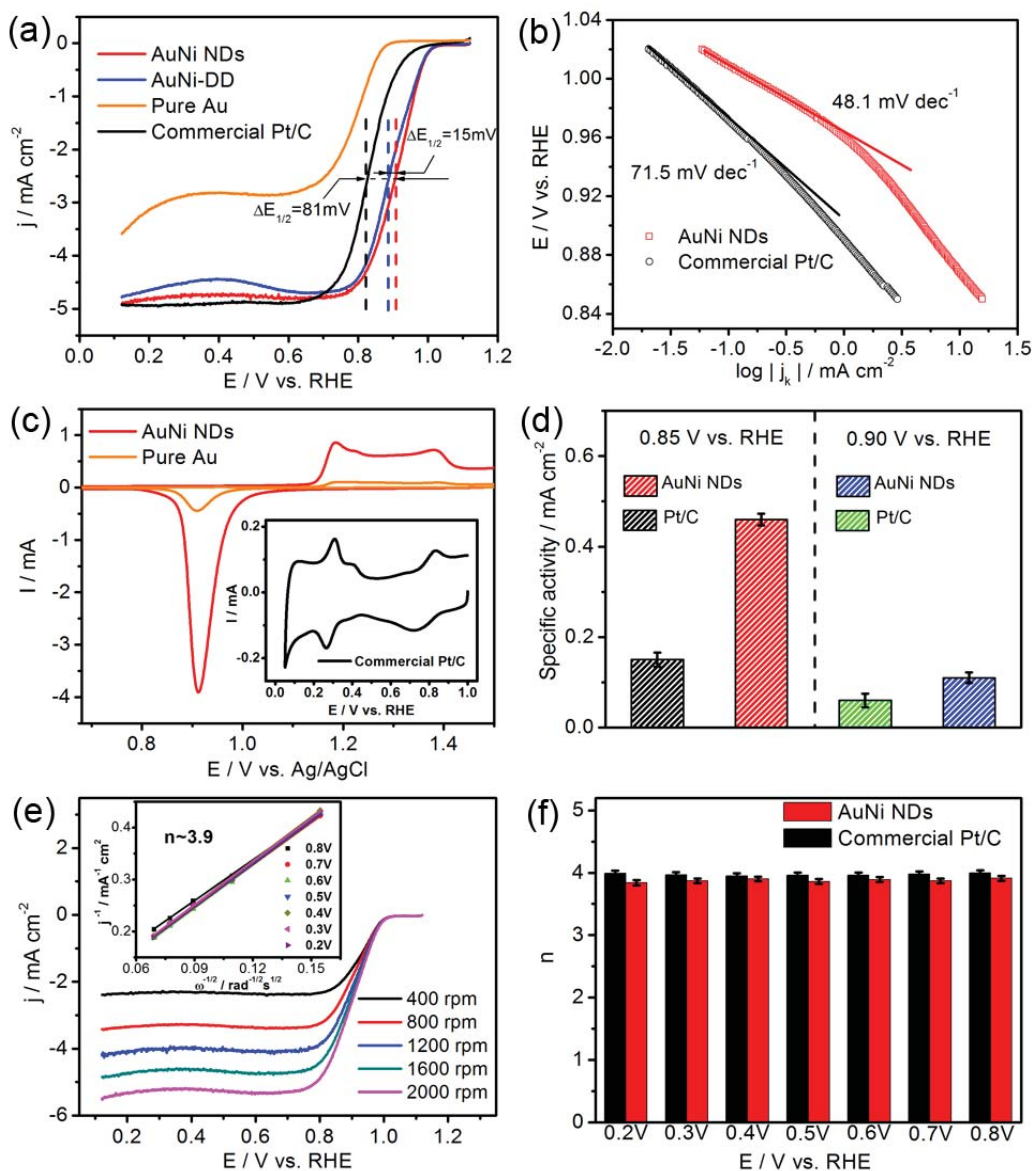
Figure 4. (a) ORR polarization curves for AuNi NDs (red line), AuNi-DD (blue line), pure Au (orange line) and the commercial Pt/C (black line) recorded in O_2-saturated 0.1 M KOH solution with a sweep rate of 10 mV s^{-1} and the RDE rotation rate of 1600 rpm. (b) Comparative mass-corrected Tafel plots for AuNi NDs and the Pt/C. (c) Cyclic voltammetry (CV) curves for AuNi NDs and pure Au recorded in N_2-saturated 0.5 M H_2SO_4 aqueous solution with a sweep rate of 50 mV s^{-1} and the Ag/AgCl electrode used as the reference electrode. The inset presents the CV curve of the commercial Pt/C catalyst recorded in N_2-saturated 0.1 M KOH solution. (d) The comparison of ORR specific activities of different catalysts at 0.85 V and 0.9 V vs. RHE, showing that the AuNi NDs deliver 3.1 times higher in specific activity than the commercial Pt/C at 0.85 V vs. RHE. (e) ORR polarization curves of AuNi NDs at different rotation rates (from 400 to 2000 rpm). The inset shows the corresponding Koutecky-Levich plots (j^{-1} vs. $\omega^{-1/2}$) of AuNi NDs at different potentials. (f) Summary of electron transfer numbers (n) of AuNi NDs and the Pt/C at various potentials, indicating that the AuNi NDs exhibit an effective four-electron pathway towards ORR. The electrocatalytic results were obtained from at least three independent measurements, and the error bars are also included in (d) and (f). In (a) and (e), current densities are normalized by the geometric area of a RDE (0.196 cm^2).
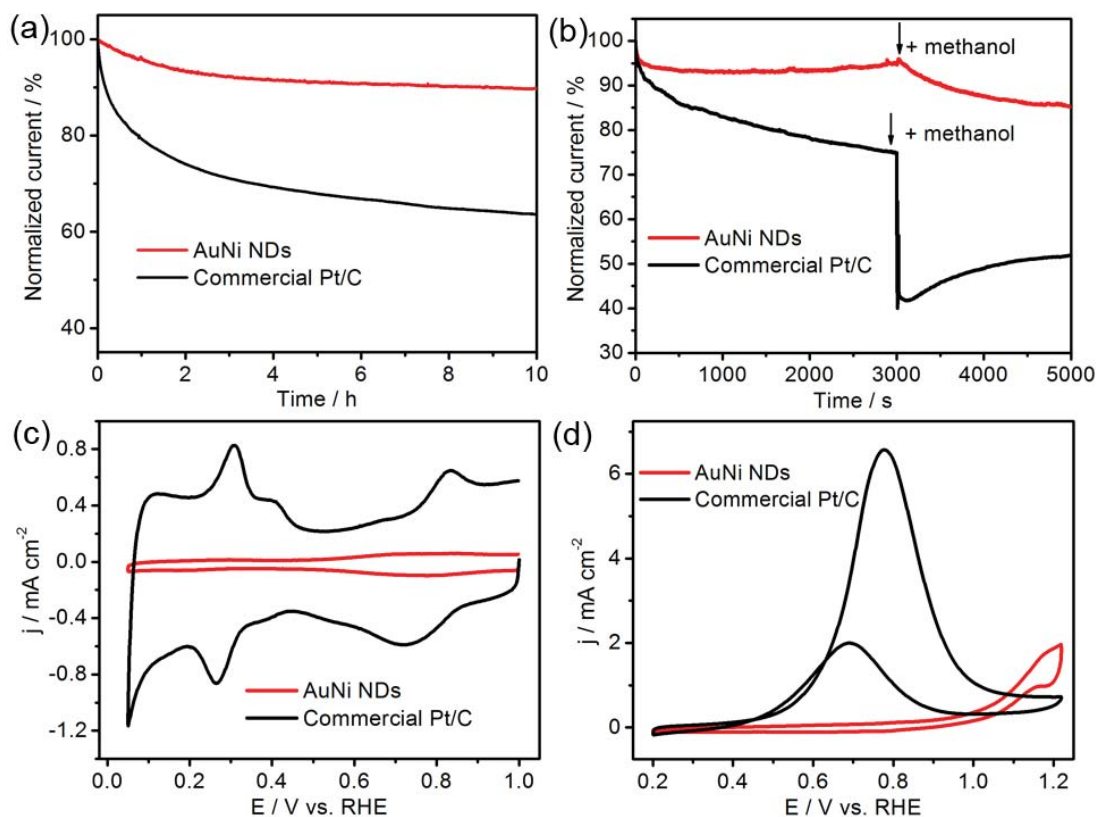
Figure 5. Chronoamperometric responses (a, b) and cyclic voltammetry curves (c, d) with and without 1 M methanol for AuNi NDs (red line) and the commercial Pt/C (black line) catalysts. (a) ORR stability test recorded in O_2-saturated 0.1 M KOH solution at a rotation rate of 1600 rpm for 10 h. (b) Methanol crossover test by introducing methanol into the 0.1 M KOH solution at 3000 s (the arrow indicates the addition of methanol). CV curves recorded (c) in N_2-saturated 0.1 M KOH solution, and (d) in N_2-saturated 0.1 M KOH + 1 M methanol with a sweep rate of 50 mV s^{-1}.
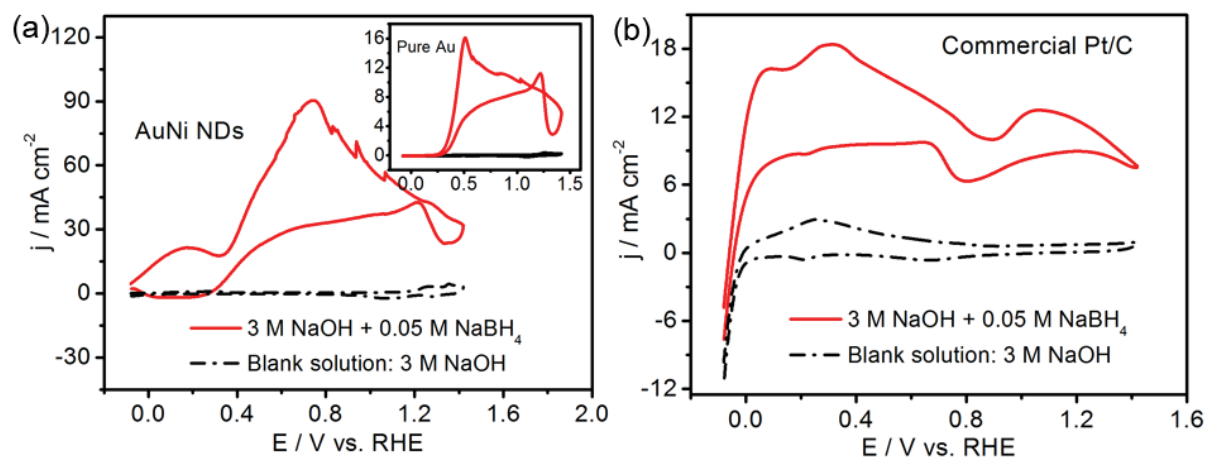
Figure 6. Electrochemical BOR performance of different electrocatalysts. CV curves of AuNi NDs (a), pure Au (inset) and the commercial Pt/C (b) catalysts recorded at room temperature in 3 M NaOH blank solution (black dashed line) and 0.05 M NaBH$_4$ + 3 M NaOH solution (red line) at a scan rate of 50 mV s^{-1}.

Table 1. The elemental compositions obtained by EDX and XPS analysis for two different AuNi catalysts synthesized by the one-pot and traditional combined methods.

catalyst	precursor Au : Ni (mM)	applied potential (V_{SCE})	EDX analysis (at %)				XPS analysis (at %)			
			before dealloying		after dealloying		before dealloying		after dealloying	
			Au	Ni	Au	Ni	Au	Ni	Au	Ni
AuNi NDs	15:30	-0.8 V	-	-	94.37	5.63	-	-	94.29	5.71
AuNi-DD[a]	15:30	-0.8 V	70.91	29.09	93.06	6.94	69.13	30.87	93.64	6.36

[a]: The applied potential in the last step during the one-pot route is -0.8 V vs. SCE, which is the same as the applied electrodeposition potential in the combined method.

Table 2. The electrochemical ORR properties for AuNi NDs, AuNi-DD and the commercial Pt/C catalysts. E_{onset}, onset potential; $E_{1/2}$, half-wave potential; j_d, diffusion-limiting current density; SA, specific activity; n, electron transfer number; SD, Standard deviation.

catalyst	E_{onset} (V) ±SD	$E_{1/2}$ (V) ±SD	j_d (mA cm^{-2}) ±SD	SA at 0.85 V (mA cm^{-2}) ±SD	Tafel (mV dec^{-1})	n
AuNi NDs	1.032±0.001	0.911±0.002	4.98±0.015	0.46±0.007	48.1	˜3.9
AuNi-DD	1.030±0.001	0.896±0.003	4.86±0.017	0.28±0.005	53.4	˜3.9
Commercial Pt/C	0.970±0.002	0.830±0.002	4.99±0.010	0.15±0.011	71.5	4.0

The first example of one-pot synthesis of dealloyed bimetallic nanostructures is proposed in which alloying and dealloying processes are precisely controlled by applying modulated potentials in the single electrolyte. The unique nanodendritic structure and tuned electronic effect enable the as-synthesized AuNi nanodendrites possess more superior bifunctional catalytic performance for oxygen reduction and borohydride oxidation than the commercial state-of-the-art Pt/C.

Keywords: one-pot synthesis, dealloyed bimetallic nanostructures, electronic effect, AuNi nanodendrites, bifunctional performance

Jiali Wang,[a] Fuyi Chen,*[a] Yachao Jin,[a] Yimin Lei,[b] and Roy L. Johnston*[c]

Dr. J. Wang, Prof. F. Chen, Dr. Y. Jin
State Key Laboratory of Solidification Processing, Northwestern Polytechnical University,
Xi'an, 710072, China
E-mail: fuyichen@nwpu.edu.cn (Fuyi Chen)

Dr. Y. Lei
School of Advanced Materials and Nanotechnology, Xidian University,
Xi'an, 710126, China

Prof. R. L. Johnston
School of Chemistry, University of Birmingham,
B15 2TT, UK
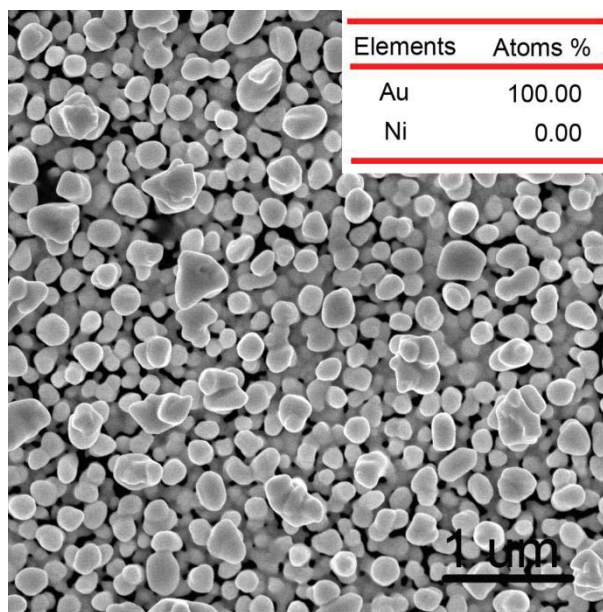E-mail: r.l.johnston@bham.ac.uk

One-pot Synthesis of Dealloyed AuNi Nanodendrite as a Bifunctional Electrocatalyst for Oxygen Reduction and Borohydride Oxidation Reaction

TOC Figure
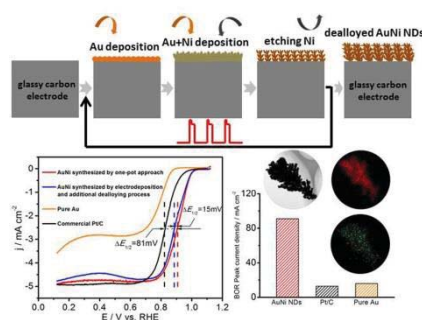
Supporting Information

One-pot Synthesis of Dealloyed AuNi Nanodendrite as a Bifunctional Electrocatalyst for Oxygen Reduction and Borohydride Oxidation Reaction

Jiali Wang,[a] Fuyi Chen,*[a] Yachao Jin,[a] Yimin Lei,[b] and Roy L. Johnston*[c]

Dr. J. Wang, Prof. F. Chen, Dr. Y. Jin
State Key Laboratory of Solidification Processing, Northwestern Polytechnical University,
Xi'an, 710072, China
E-mail: fuyichen@nwpu.edu.cn (Fuyi Chen)

Dr. Y. Lei
School of Advanced Materials and Nanotechnology, Xidian University,
Xi'an, 710126, China

Prof. R. L. Johnston
School of Chemistry, University of Birmingham,
B15 2TT, UK
E-mail: r.l.johnston@bham.ac.uk

Elements	Atoms %
Au	100.00
Ni	0.00

Figure S1. SEM image of the pure Au catalyst synthesized by the same one-pot approach, exhibiting the nanoparticle feature of the pure Au. Inset shows the corresponding EDX analysis. The pure Au sample was prepared at -0.8 V vs. SCE in the last step by using the electrolyte without $NiSO_4$, and keeping the other conditions the same.
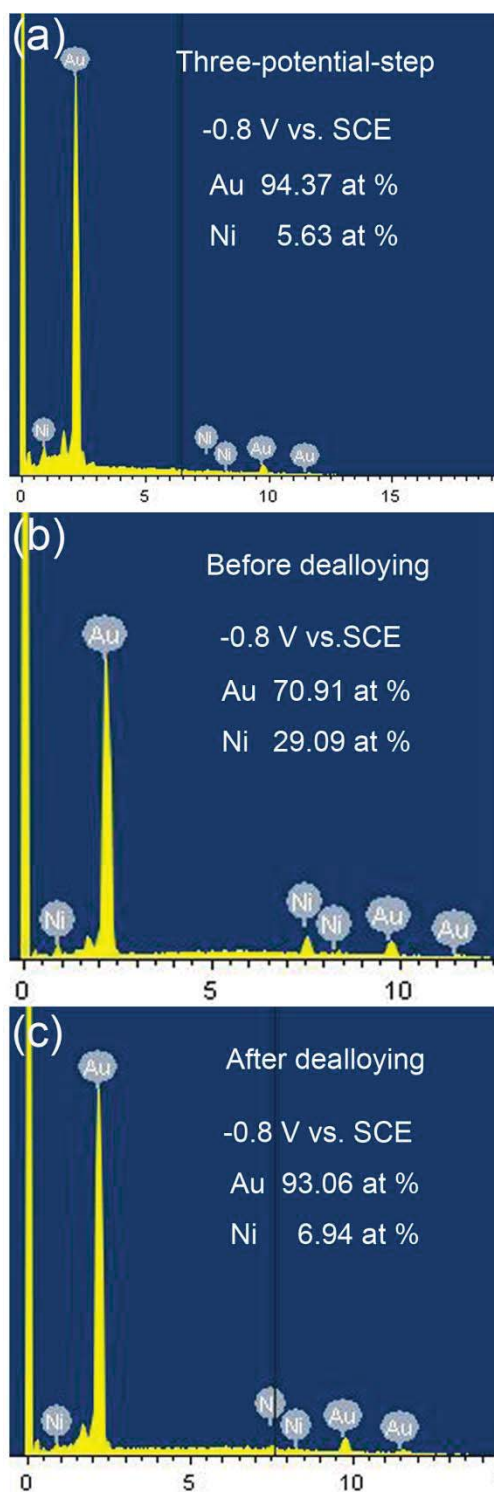
Figure S2. EDX spectra of the AuNi catalysts synthesized by two different methods. (a) AuNi NDs prepared via the one-pot approach, the potential in the last step during the three-potential-step process was set at -0.8 V vs. SCE. (b, c) AuNi catalyst (b) before dealloying and (d) after dealloying process via the traditional combined method, namely, electrodeposition and subsequent dealloying process. The electrochemical deposition potential was also set at -0.8 V vs. SCE. The Ni contents in both AuNi NDs (a) and AuNi-DD (c) catalysts are comparable, indicating that the one-pot strategy could effectively etching Ni atoms out of the AuNi bimetallic nanodendrites, and is even more powerful than the traditional combined method.
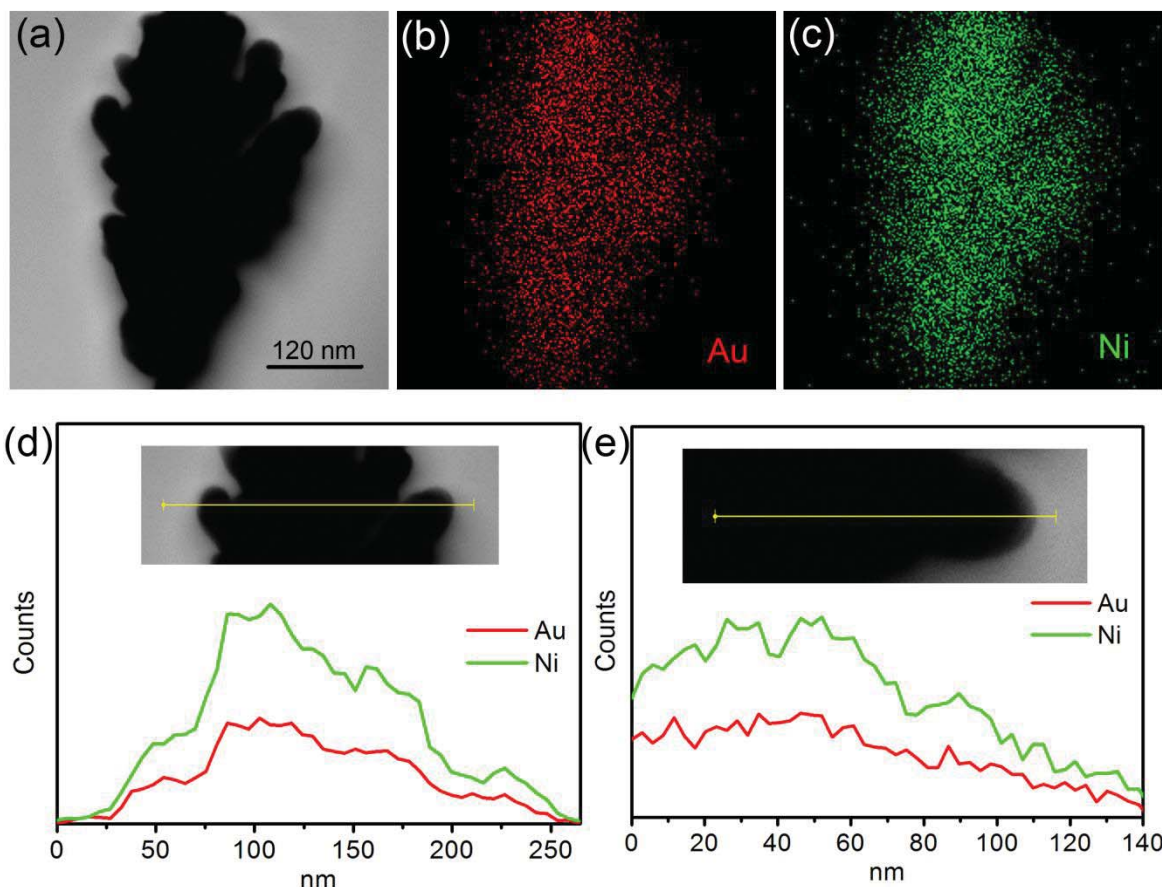
Figure S3. (a) Bright field TEM image of an individual AuNi nanodendrite synthesized at -1.0 V vs. SCE in the last step for analysis, showing the coarse nanodendrite nature of AuNi catalyst prepared at the more negative voltage. (b, c) EDX elemental mapping for the individual elements. Red indicates Au and green indicates Ni. Based on the location and intensity, the result presents that the amount of Ni is higher than that of Au in the AuNi NDs when the applied potential drops to -1.0 V vs. SCE, and the uniform distribution of Au and Ni could also be easily achieved by using the novel one-pot synthetic route. (d, e) EDX line-scanning profiles taken at the positions indicated in the insets, showing the formation of the Ni-rich surface.
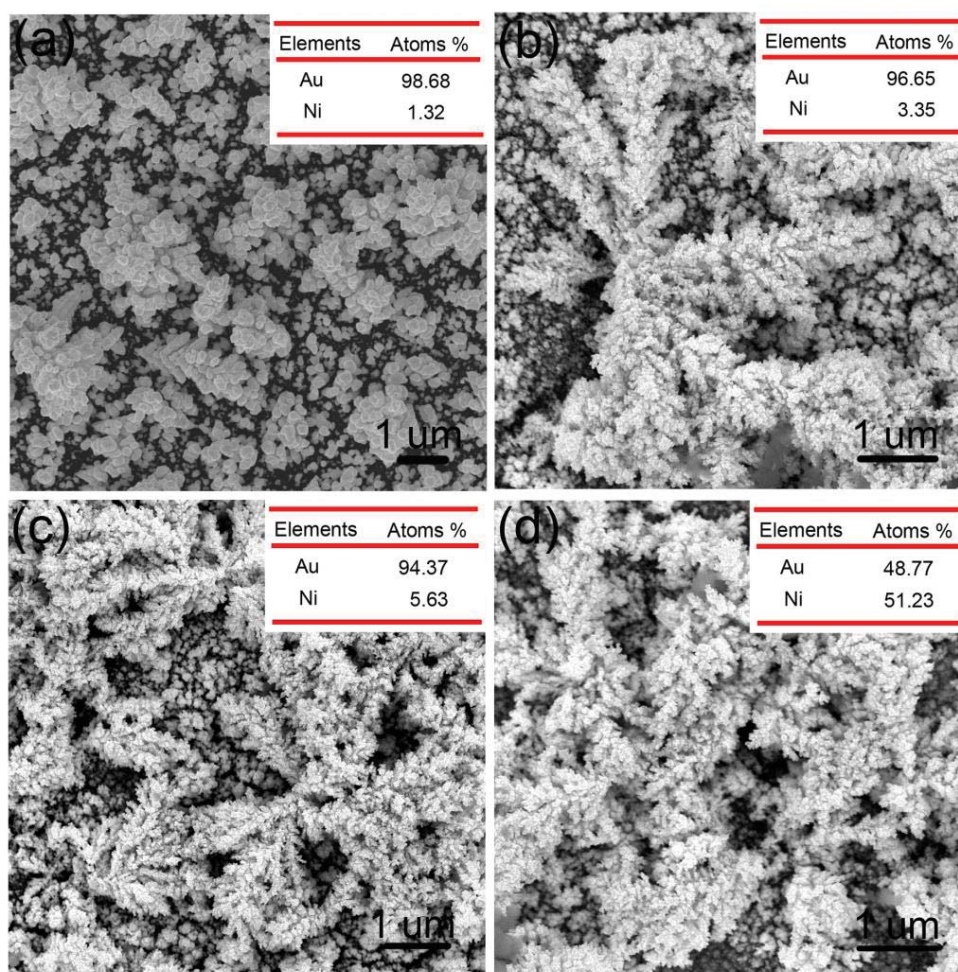
Figure S4. SEM images of the AuNi NDs synthesized at different voltage values in the last step. (a) -0.6 V, (b) -0.7 V, (c) -0.8 V and (d) -1.0 V vs. SCE. Inset in (a-d) shows the corresponding EDX analysis.

It can be seen that the Ni content in the AuNi NDs greatly improves with the applied potential going more negative (i.e., 51.23 at % at -1.0 V vs. SCE). This is mainly because the preformed Au nanoparticles used as nucleic centers for Ni atoms makes them easier to be reduced, which is known as the underpotential deposition.[1] Compared to the pure Au, all the AuNi catalysts show the nanodendrite feature, confirming the element Ni plays an important role in controlling the morphology of the bimetallic nanostructures under our experimental conditions. The appropriate Ni content in the AuNi NDs would facilitate the formation of well-developed nanodendrites. The AuNi NDs synthesized at -0.8 V vs. SCE exhibit the optimized morphology among all the catalysts, thus exposing more active sites for the oxygen reduction.

34
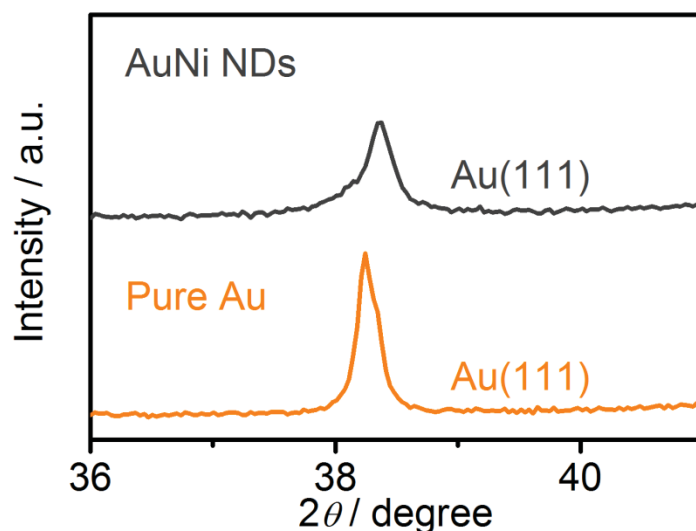
Figure S5. Enlarged peaks of Au (111) plane for AuNi NDs and pure Au samples between 38° and 39°. The Au (111) peak of the AuNi NDs is slightly positive-shifted (around +0.07 degree) compared to the pure Au.

Based on the Bragg equation, the interplanar spacings of Au (111) plane are 0.2351 and 0.2347 nm for pure Au and AuNi NDs, respectively. It can be noted that the lattice contraction for AuNi NDs is only 0.17 % compared to the pure Au sample, much less than that of previously reported alloy systems,[2] which suggests that the AuNi NDs are composed of Au and Ni metals with insignificant amount of AuNi alloys formed.
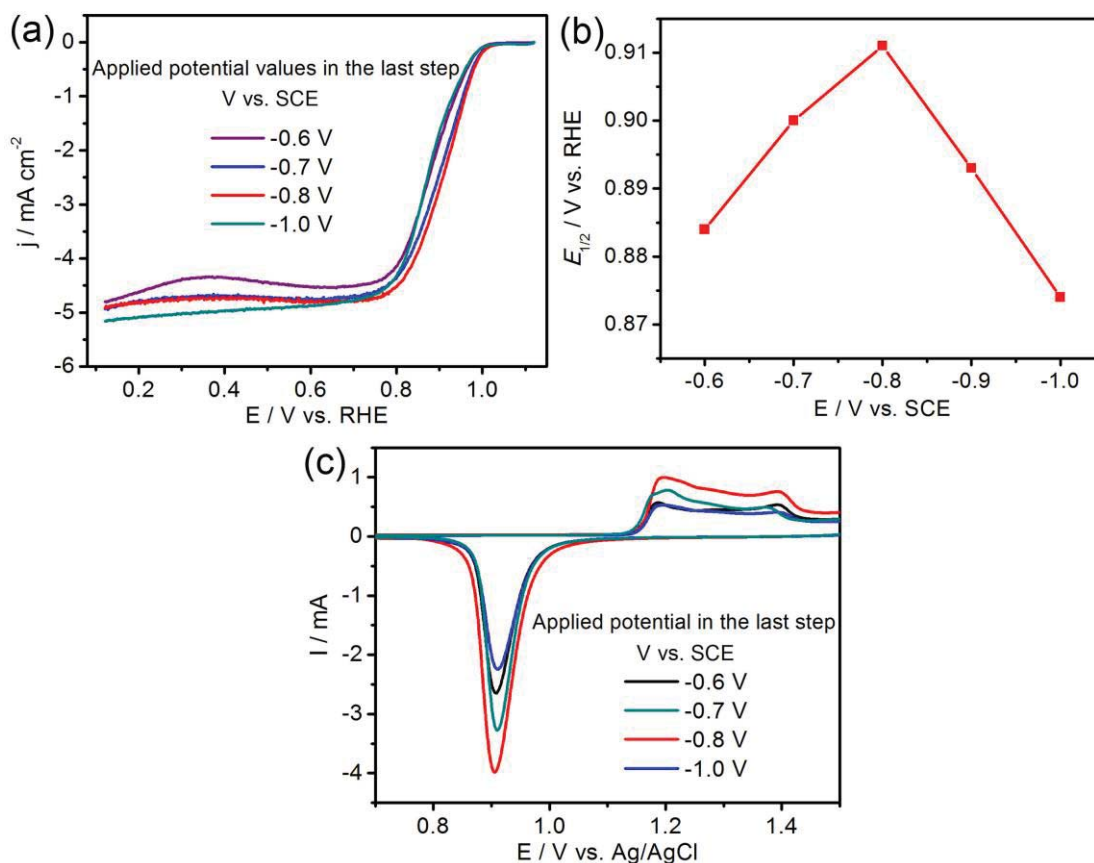
Figure S6. (a) ORR polarization curves of the AuNi NDs synthesized under different potential values in the last step during the periodic three-potential-step program (Sweep rate: 10 mV s^{-1}; RDE rotation rate: 1600 rpm). The LSV curve of the AuNi catalyst synthesized at -0.9 V vs. SCE is omitted for clarity in (a). (b) The parabolic relation between the applied potential value and the half-wave potential ($E_{1/2}$), the above result provides a direct evidence supporting critical role of Ni contents for the ORR electrocatalysis. (c) Cyclic voltammetry (CV) curves for AuNi NDs synthesized at different potential values recorded in N$_2$-saturated 0.5 M H$_2$SO$_4$ aqueous solution with a sweep rate of 50 mV s^{-1}. The AuNi NDs synthesized at -0.8 V vs. SCE exhibit the highest ECSA, meanwhile, the AuNi catalyst synthesized at -1.0 V vs. SCE presents the lowest ECSA, mainly due to the excessive Ni coverage on the active sites.

The SEM images (Figure S4) and comparative LSV curves (Figure S6a) of the AuNi NDs synthesized under different voltage values in the last step show that the Ni content plays a crucial role in the growth of nanostructured dendrites and thus the oxygen reduction electrocatalysis. Firstly, as shown in Figure S4 and Table S1, the Ni content in AuNi NDs increases from 1.32 to 51.23 at % with the applied potential in the last step changing from -0.6 to -1.0 V vs. SCE, simultaneously leading to the morphological variation of the AuNi

samples. Typically, compared to the pure Au sample in Figure S1, Figure S4a shows the clear aggregated AuNi nanoparticles by introducing very little element Ni. As shown in Figure S4b and 4c, the appropriate Ni content facilitates the formation of hierarchical dendritic nanostructure with higher level of porosity, in particular, the AuNi catalyst synthesized at -0.8 V vs. SCE consists of dense nanodendrite with relatively high yield (Figure S4c). AuNi catalyst retains its dendritic morphology when the voltage reaches -1.0 V vs. SCE (Figure S4d), but its coursing and collapse are visible. The structure and elemental distribution of the AuNi NDs synthesized at the -1.0 V vs. SCE in the last step are shown in Figure S3, it can be seen that Au and Ni are still uniformly distributed, meanwhile, the nanodendritic surface has changed from the Au-rich to the Ni-rich state. As a result, AuNi NDs prepared at -0.8 V vs. SCE exhibit the highest electrochemically active surface area (ECSA) among all the samples (red line in Figure S6c), effectively improving the catalytic activity towards ORR. As shown in Figure S6b, with the applied voltage values going more negative (from -0.6 to -0.8 V vs. SCE), the AuNi NDs exhibit a remarkable increase trend in half-wave potential ($E_{1/2}$), and reach the maximum value at -0.8 V vs. SCE (0.911 V). Afterwards, the half-wave potential values show a depressed trend upon furthering the applied voltage, at -1.0 V vs. SCE, the $E_{1/2}$ value decreases to 0.874 V vs. RHE. These results indicate that the most efficient catalytic oxygen reduction reaction could be achieved by grafting ORR catalysts with appropriate amount of Ni contents. Excessive Ni content in AuNi NDs would make active sites easily covered to some extent and reduces the catalytic activity for the ORR. On the other hand, less Ni content also has a negative effect on the ORR catalysis, might due to the weaker electronic effect between Au and Ni atoms.
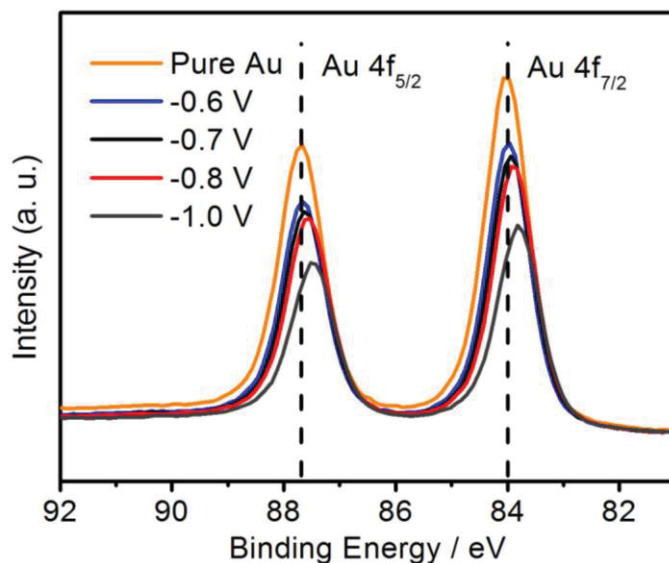
Figure S7. Au 4f$_{7/2}$ XPS spectra of different AuNi catalysts synthesized at various potentials (from -0.6 to -1.0 V vs. SCE), with pure Au being included as the baselines.

As shown in Figure S7, the Au 4f$_{7/2}$ shifts to the lower binding energies upon forming the interaction with Ni atoms compared to the pure Au catalyst. It also can be seen that the more the Ni content is in the AuNi catalysts, the stronger the shift is, which indicates the stronger upshift of the d-band center of Au with respect to the Fermi level and thus the higher adsorption energy of oxygen. However, the excessive Ni contents in the AuNi catalysts would seriously block the Au active sites on the surface, resulting in the degradation of their ORR activities. The AuNi catalyst with the Ni content of 5.71 at % (examined by the XPS, Table S1) showing the best catalytic activity highlights that the appropriate Ni content in the AuNi catalyst could not only effectively modify the electronic structure leading to higher oxygen adsorption energy but also keep sufficient Au active sites exposing to the reactants.
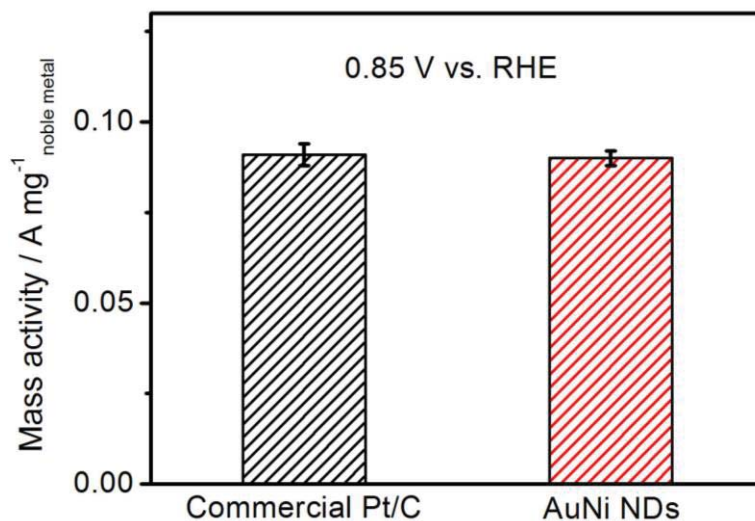
Figure S8. The comparison of ORR mass activities of AuNi NDs and commercial Pt/C catalysts at 0.85 V vs. RHE, showing that the AuNi NDs catalyst exhibits a comparable ORR mass activity to the commercial Pt/C at 0.85 V vs. RHE.
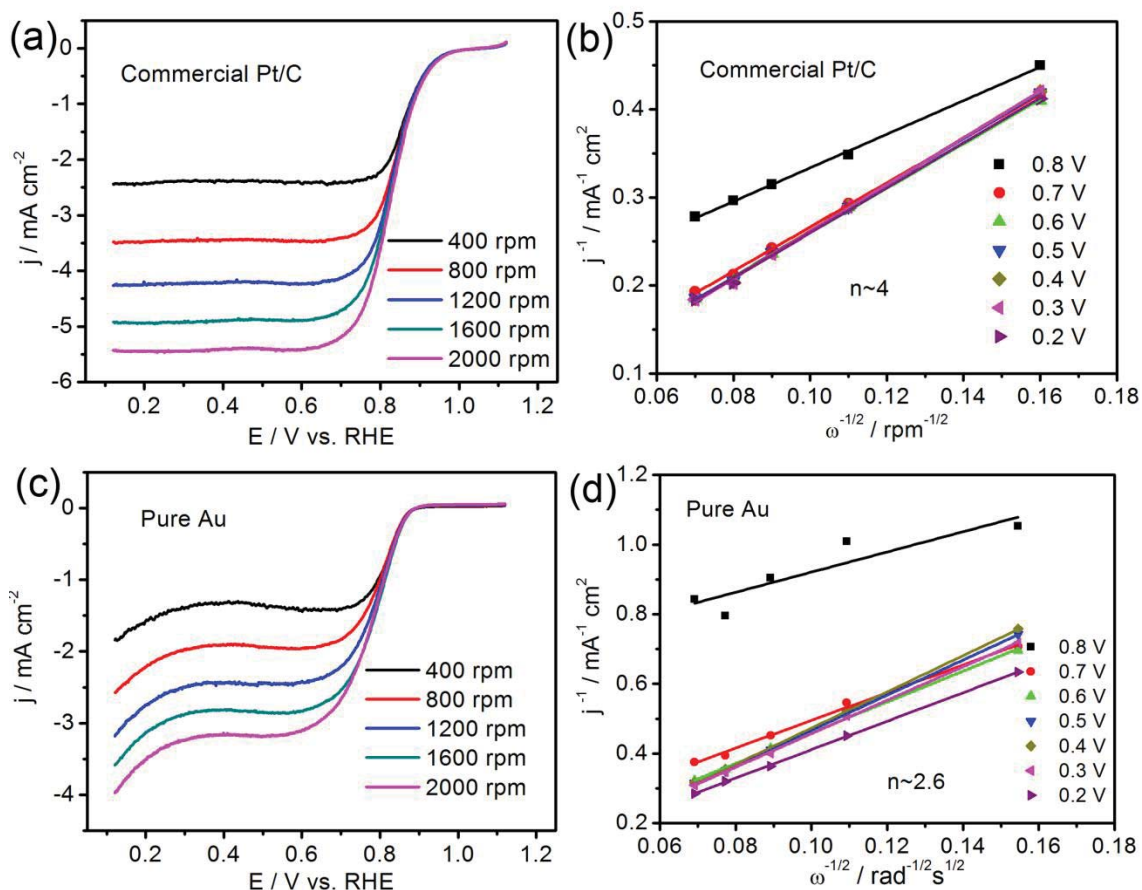
Figure S9. The rotation-rate-depend LSV curves of (a) the commercial state-of-the-art Pt/C catalyst and (c) pure Au recorded in O_2-saturated 0.1 M KOH aqueous solution with a sweep rate of 10 mV s^{-1} at different rotation rate ranging from 400 to 2000 rpm. (b, d) The corresponding Koutecky-Levich plots ((j^{-1} vs. $\omega^{-1/2}$) at different voltage values for the commercial Pt/C and pure Au catalyst, respectively.

As shown in Figure 4e, Figure S9a and 9c, all the catalytic current densities increase with an increase in the rotating rates (from 400 to 2000 rpm), indicating that the catalytic oxygen reduction is controlled by the mass transport of oxygen molecular to the surface of electrode. Furthermore, the corresponding Koutecky-Levich plots ((j^{-1} vs. $\omega^{-1/2}$) show the good linearity over the voltages range from 0.2 to 0.8 V vs. RHE, which confirms a first-order reaction with respect to the dissolved oxygen molecular. The electron transfer numbers (n) from the slope of the linear fit lines are calculated to be 4 and 2.6 for the commercial Pt/C and pure Au catalyst, respectively, indicating that the oxygen reduction catalyzed by the pure Au catalyst proceeds via the two-electron and four-electron parallel reaction pathways, while the ORR by the commercial Pt/C catalyst is considered to be an absolute four-electron reaction.
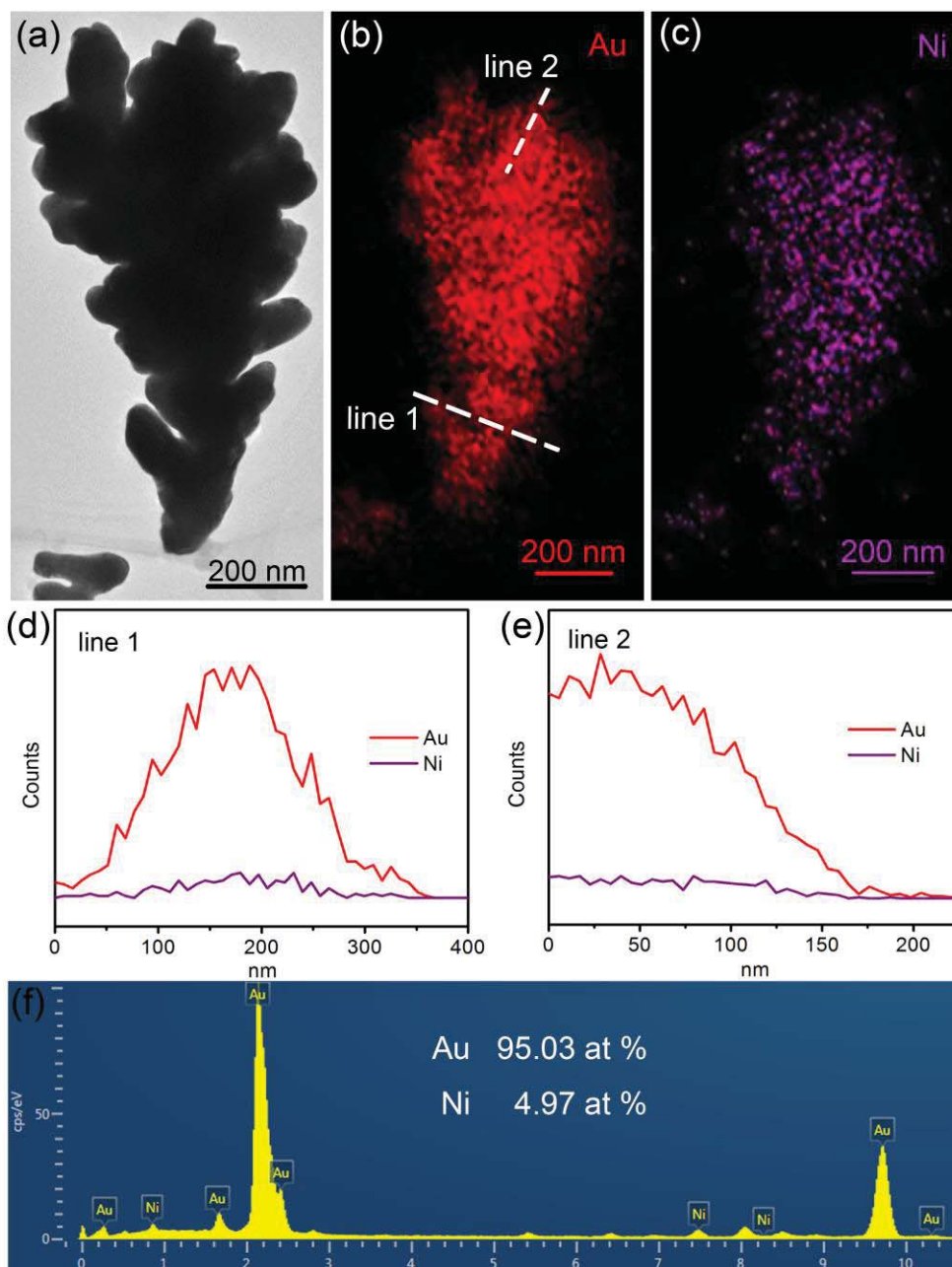
Figure S10. General characterization of the AuNi NDs after the long-term (10 hours) stability test. (a) Bright field TEM image of the AuNi NDs. (b, c) EDX elemental mapping of a single representative nanodendrite. Red represents Au, and purple represents Ni. (d, e) EDX line profiles extracted from two typical lines in (b). (f) The corresponding EDX composition analysis of AuNi catalyst.
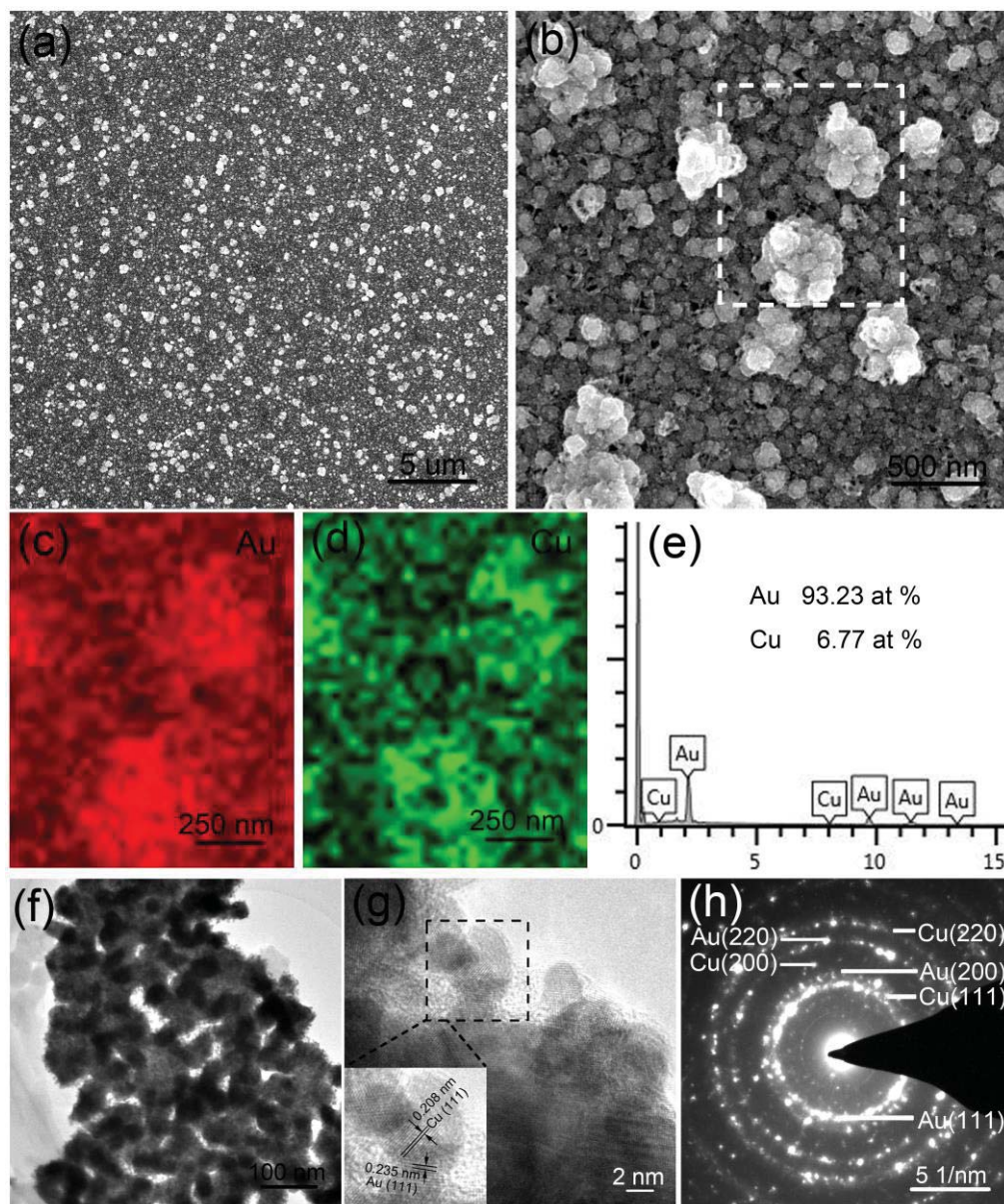
Figure S11. General characterization of the dealloyed AuCu electrocatalyst synthesized by the one-pot strategy in the single electrolyte solution. (a, b) SEM images of the AuCu catalyst (c, d) EDX elemental mapping of the representative nanoparticles. Red represents Au, and green represents Cu. Both Au and Cu are distributed uniformly in the AuCu catalyst. (e) The corresponding EDX compositional analysis of AuCu catalyst. (f) Bright field TEM images of the AuCu catalyst. (g) HRTEM image of the dealloyed AuCu, the inset shows the magnified image obtained in the framed part (dashed frame). (h) SAED pattern of the dealloyed AuCu catalyst.
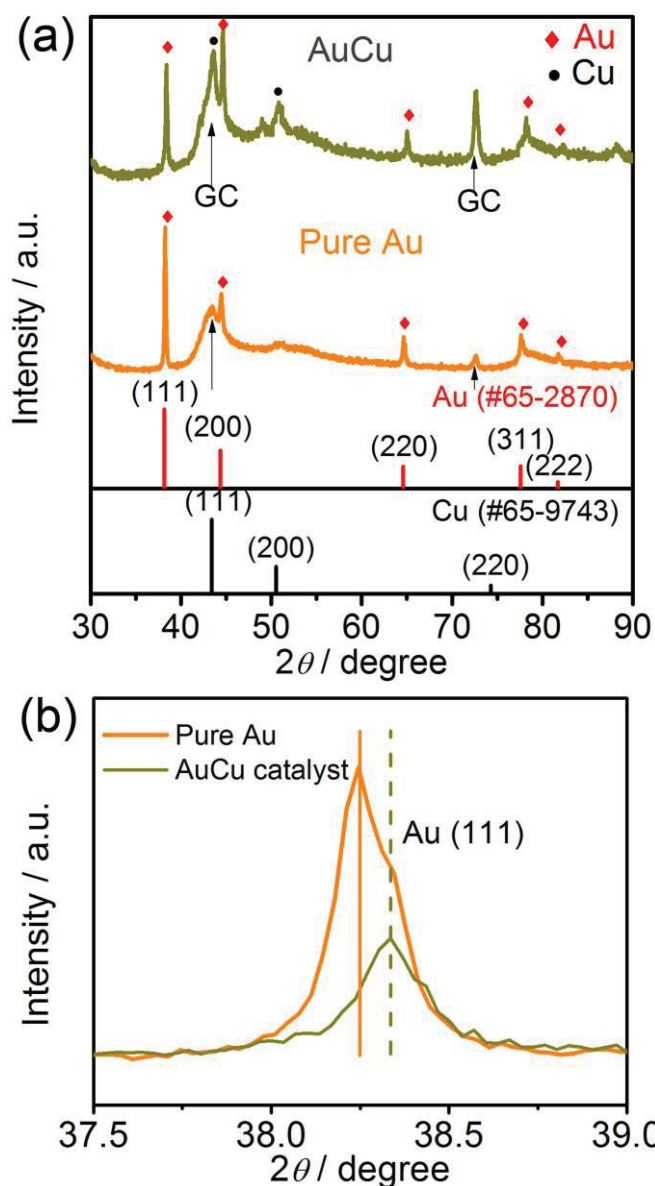
Figure S12. (a) XRD patterns for the AuCu electrocatalyst and pure Au samples. Bar diagram: Au #65-2870, Cu #65-9743. (b) Enlarged peaks of Au (111) plane for the AuCu and pure Au samples between 37.5° and 39°. The Au (111) peak of the AuCu catalyst is slightly positive shifted (only 0.08 degree) compared to the pure Au.
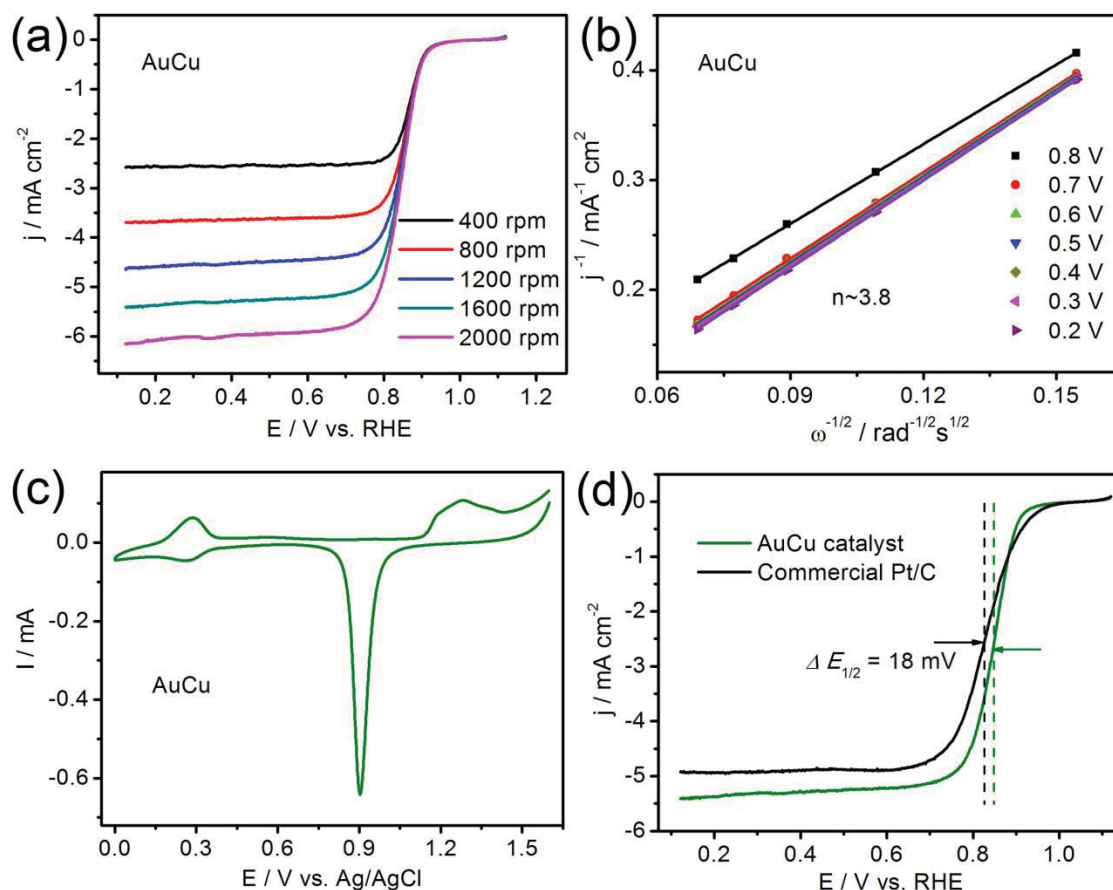
Figure S13. (a) The rotation-rate-depend LSV curves of AuCu electrocatalyst recorded in O_2-saturated 0.1 M KOH aqueous solution with a sweep rate of 10 mV s^{-1} at different rotation rate ranging from 400 to 2000 rpm. The AuCu catalyst was also prepared via the same three-potential-step route, and $NiSO_4$ was replaced by the $CuSO_4$ in the electrolyte. (b) The corresponding Koutecky-Levich plot ((j^{-1} vs. $\omega^{-1/2}$) at different voltage values for the as-synthesized AuCu catalyst. The electron transfer number (n) is calculated to be around 3.8, also showing that the ORR catalyzed by the AuCu catalyst mainly proceeds via the four-electron pathway. (c) CV curve of the as-synthesized AuCu catalysts recorded in N_2-saturated 0.5 M H_2SO_4 aqueous solution with a sweep rate of 50 mV s^{-1}, and the Ag/AgCl electrode used as the reference electrode. The ECSA of the as-synthesized AuCu catalyst can be calculated by integrating the charge between 0.6 and 1.0 V vs. Ag/AgCl. (d) ORR polarization curves of the AuCu and commercial Pt/C catalysts, recorded in O_2-saturated 0.1 M KOH solution with a sweep rate of 10 mV s^{-1} and the rotation rate of 1600 rpm. The as-prepared AuCu catalyst shows improved catalytic activity towards ORR, around a 18 mV positive shift in half-wave potential ($E_{1/2}$) and 2.7 times enhancement in specific activity with respect to the commercial state-of-the-art Pt/C catalyst. In addition, for the AuCu catalyst, the current reaches its diffusion-limited value of 5.5 mA cm^{-2}, higher than that of the Pt/C (~ 5.0 mA cm^{-2}).
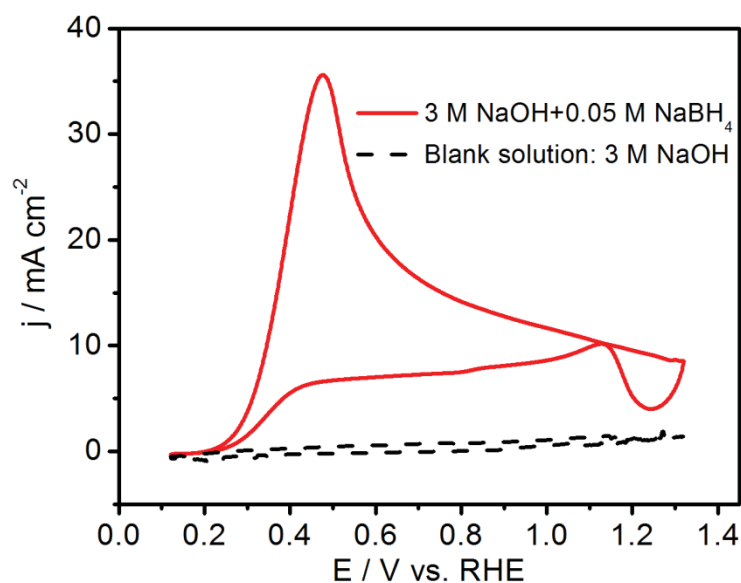
Figure S14. CV curve of the as-synthesized AuCu electrocatalyst recorded at room temperature in 3 M NaOH blank solution (black dashed line) and 0.05 M $NaBH_4$ + 3 M NaOH solution (red line) at a scan rate of 50 mV s^{-1}.

The electrochemical BOR activity of the identically synthesized AuCu catalyst by the one-pot approach was evaluated by the CV curve. It can be seen that the AuCu catalyst shows the higher oxidation current density and more negative onset potential towards BOR than the commercial Pt/C.

Table S1. The EDX and XPS composition analysis, measured Au $4f_{7/2}$ electron binding energies, and the half-wave potentials of different AuNi catalysts synthesized at various potentials.

Applied potential at the last step (V vs. SCE)	EDX bulk composition		XPS surface composition		Binding energy (eV)	Half-wave potential (V vs. RHE)
	Au (at %)	Ni (at %)	Au (at %)	Ni (at %)	Au $4f_{7/2}$	
-0.8 V	100.00	0.00	100.00	0.00	84.07	0.790
-0.6 V	98.68	1.32	98.83	1.17	84.05	0.884
-0.7 V	96.65	3.35	96.97	3.03	84.03	0.900
-0.8 V	94.37	5.63	94.29	5.71	83.97	0.911
-1.0 V	48.77	51.23	49.07	50.93	83.87	0.874

Table S2. Comparison of the ORR catalytic performance of the optimized AuNi NDs with other electrocatalysts in the scientific literature (at the electrode rotation rate of 1600 rpm). E_{onset}, onset potential; $E_{1/2}$, half-wave potential; $\Delta E_{1/2}$, the difference of half-wave potential ($E_{1/2}$) between the reported catalyst and the commercial Pt/C, the positive value represents the improvement in $E_{1/2}$ with respect to Pt/C, the minus value represents the opposite trend; SA, specific activity; IF, defined as the ratio of specific activity of the proposed catalyst divided by that of the identically synthesized commercial Pt/C, measured at the same voltage.

Catalyst	E_{onset} (V)	$E_{1/2}$ (V)	$\Delta E_{1/2}$ (mV)	SA (mA cm^{-2})	Measured at (V)	IF	Temp.	Electrolyte	Ref.
AuNi NDs	1.032	0.911	**81**	0.460	0.85	**3.1**	RT	0.1 M KOH	this work
Pure Au NPs	0.886	0.790	-40	-	-	-	RT	0.1 M KOH	this work
AuCu	0.960	0.848	18	0.40	0.85	2.7	RT	0.1 M KOH	this work
Dealloyed AuNi	1.030	0.896	67	0.500	0.80	2.8	RT	0.1 M KOH	[3]
AuNi	1.000	0.869	40	0.430	0.80	2.4	RT	0.1 M KOH	[3]
Pure Au	0.900	0.810	-19	0.150	0.80	-	RT	0.1 M KOH	[3]
Dealloyed AuNi@pTBA*	-	0.884	40	0.590	0.82	2.1	RT	0.1 M NaOH	[4]
AuNi@pTBA*	-	0.824	-20	0.290	0.82	1.0	RT	0.1 M NaOH	[4]
AuAg	0.917	-	-	-	-	-	RT	0.1 M NaOH	[5]
Au/rGO	-	0.610	-20	-	-	-	RT	0.1 M KOH	[6]
Au$_{67}$Pd$_{33}$/CNs	0.940	0.830	-	-	-	-	RT	0.1 M KOH	[7]
Au$_{0.9}$Pd$_{0.1}$/C**	0.958	0.858	-12	-	-	-	RT	0.1 M NaOH	[8]
Au$_{0.8}$Pd$_{0.2}$/C**	1.043	0.911	41	-	-	-	RT	0.1 M NaOH	[8]
Au$_{0.7}$Pd$_{0.3}$/C**	0.993	0.872	2	-	-	-	RT	0.1 M NaOH	[8]
Au(100)	0.960	0.800	-	-	-	-	RT	0.1 M KOH	[9]
Au(110)	0.840	0.700	-	-	-	-	RT	0.1 M KOH	[9]
Au(111)	0.840	0.670	-	-	-	-	RT	0.1 M KOH	[9]
Dealloyed Pt$_6$Ni$_1$	-	0.916	50	1.230	0.90	6.2	30°C	0.1 M HClO$_4$	[10]
Dealloyed Pt$_1$Ni$_1$	-	0.897	31	0.670	0.90	3.4	30°C	0.1 M HClO$_4$	[10]
Dealloyed Pt$_{15}$Cu$_{85}$	-	0.890	30	0.450	0.90	3.0	RT	0.1 M HClO$_4$	[11]
Dealloyed PtFe$_5$	-	-	-	0.383	0.90	2.3	25°C	0.1 M HClO$_4$	[12]
Dealloyed PdCu	-	0.840	15	0.150	0.80	1.5	RT	0.1 M HClO$_4$	[13]
Dealloyed PdNi	-	-	-	0.210	0.90	1.3	RT	0.1 M HClO$_4$	[14]

All of the potentials in this table were referred to RHE unless indicated. * represents that the V_{RHE} was converted from Ag/AgCl saturated KCl, $E_{vs.\ RHE} = E_{vs.\ Ag/AgCl} + 0.197\ V + 0.059 \times$ PH. ** represents that the V_{RHE} was converted from saturated calomel electrode, $E_{vs.\ RHE} = E_{vs.\ SCE} + 0.241\ V + 0.059 \times$ PH.

Table S3. Comparison of the BOR catalytic activity of our optimized AuNi NDs with other AuNi nanostructures and state-of-the-art BOR electrocatalysts reported in the recent literature.

Catalyst	Peak potential	Peak current density (mA cm^{-2})	Reference electrode	Scan rate (mV s^{-1})	Electrolyte	Ref.
AuNi NDs	0.700	**91.00**	RHE	50	3 M NaOH + 0.05 M NaBH$_4$	this work
Au NPs	-0.530	16.00	RHE	50	3 M NaOH + 0.05 M NaBH$_4$	this work
Pt/C	1.100	13.00	RHE	50	3 M NaOH + 0.05 M NaBH$_4$	this work
Au Ncage/G	0.100	-	SCE	50	3 M NaOH + 0.10 M NaBH$_4$	[15]
Ni$_1$@Au$_1$/C	-0.190	26.00	MOE	50	1 M NaOH + 0.03 M NaBH$_4$	[16]
Au/C	-0.040	16.00	MOE	50	1 M NaOH + 0.03 M NaBH$_4$	[16]
Au$_{45}$Co$_{55}$/C	-0.100	38.50	Ag/AgCl	20	3 M NaOH + 0.10 M NaBH$_4$	[17]
Au$_{41}$Ni$_{59}$/C	-0.322	-	Ag/AgCl	20	3 M NaOH + 0.05 M NaBH$_4$	[18]
Cu/Ni/AuNi	-	31.00	SCE	100	2 M NaOH + 0.02 M NaBH$_4$	[19]
flat Au	-	5.20	SCE	100	2 M NaOH + 0.02 M NaBH$_4$	[19]
Pt$_{67}$Sn$_{33}$/C	0.100	34.10	Ag/AgCl	20	3 M NaOH + 0.10 M NaBH$_4$	[20]
Ni$_{95}$Dy$_5$	0.400	3.70	RHE	100	2 M NaOH + 0.03 M NaBH$_4$	[21]
Co/Co$_3$O$_4$	-0.400	70.00	Ag/AgCl	20	2 M NaOH + 0.20 M NaBH$_4$	[22]
PtCo/Co$_3$O$_4$	-0.400	850.00	Ag/AgCl	20	2 M NaOH + 0.20 M NaBH$_4$	[22]
Pt$_{67}$Co$_{33}$	-	32.47	Ag/AgCl	20	3 M NaOH + 0.10 M NaBH$_4$	[23]

Abbreviations: ND, nanodendrite; NP, nanoparticle; Ncage, nanocage; G, graphene; RHE: reversible hydrogen electrode; SCE: saturated calomel electrode; MOE: Hg/HgO electrode.

[1] K.-H. Choi, Y. Jang, D. Y. Chung, P. Seo, S. W. Jun, J. E. Lee, M. H. Oh, M. Shokouhimehr, N. Jung, S. J. Yoo, *Chem. Commun.* **2016**, *52*, 597.

[2] a) D. Wang, H. L. Xin, R. Hovden, H. Wang, Y. Yu, D. A. Muller, F. J. Disalvo, H. D. Abruña, *Nat. Mater.* **2013**, *12*, 81; b) P. Strasser, S. Koh, T. Anniyev, J. Greeley, K. More, C. Yu, Z. Liu, S. Kaya, D. Nordlund, H. Ogasawara, *Nat. Chem.* **2010**, *2*, 454.

[3] J. Wang, F. Chen, Y. Jin, R. L. Johnston, *J. Mater. Chem. A* **2016**, *4*, 17828.

[4] M. H. Naveen, N. G. Gurudatt, H. B. Noh, Y. B. Shim, *Adv. Funct. Mater.* **2016**, *26*, 1590.

[5] Y. Journal of Physical Chemistry Ajournal of Physical Chemistry Asong, K. Liu, S. Chen, *Langmuir* **2012**, *28*, 17143.

[6] X.-R. Li, X.-L. Li, M.-C. Xu, J.-J. Xu, H.-Y. Chen, *J. Mater. Chem. A* **2014**, *2*, 1697.

[7] W. Yan, Z. Tang, L. Wang, Q. Wang, H. Yang, S. Chen, *Int. J. Hydrogen Energy* **2016**.

[8] A. Cha, J. H. Shim, A. Jo, S. C. Lee, Y. Lee, C. Lee, *Electroanalysis* **2014**, *26*, 723.

[9] a) R. Adžić, S. Strbac, N. Anastasijević, *Mater. Chem. Phys.* **1989**, *22*, 349; b) X. Ge, A. Sumboja, D. Wuu, T. An, B. Li, F. T. Goh, T. A. Hor, Y. Zong, Z. Liu, *ACS Catal.* **2015**, *5*, 4643.

[10] R. Wang, C. Xu, X. Bi, Y. Ding, *Energy Environ. Sci.* **2012**, *5*, 5281.

[11] X. Ge, L. Chen, J. Kang, T. Fujita, A. Hirata, W. Zhang, J. Jiang, M. Chen, *Adv. Funct. Mater.* **2013**, *23*, 4156.

[12] J. L. Shui, C. Chen, J. Li, *Adv. Funct. Mater.* **2011**, *21*, 3357.

[13] C. Xu, Y. Zhang, L. Wang, L. Xu, X. Bian, H. Ma, Y. Ding, *Chem. Mater.* **2009**, *21*, 3110.

[14] C. Xu, Y. Liu, Q. Hao, H. Duan, *J. Mater. Chem. A* **2013**, *1*, 13542.

[15] R. Valiollahi, R. Ojani, J.-B. Raoof, *Electrochim. Acta* **2016**, *191*, 230.

[16] D. Duan, J. Liang, H. Liu, X. You, H. Wei, G. Wei, S. Liu, *Int. J. Hydrogen Energy*

2015, *40*, 488.

[17]   F. Pei, Y. Wang, X. Wang, P. He, Q. Chen, X. Wang, H. Wang, L. Yi, J. Guo, *Int. J.*
         Hydrogen Energy **2010**, *35*, 8136.

[18]   P. He, Y. Wang, X. Wang, F. Pei, H. Wang, L. Liu, L. Yi, *J. Power Sources* **2011**, *196*,
         1042.

[19]   M. G. Hosseini, M. Abdolmaleki, F. Nasirpouri, *Electrochim. Acta* **2013**, *114*, 215.

[20]   L. Yi, L. Liu, X. Wang, X. Liu, W. Yi, X. Wang, *J. Power Sources* **2013**, *224*, 6.

[21]   D. Santos, B. Šljukić, L. Amaral, J. Milikić, C. Sequeira, D. Macciò, A. Saccone,
         Electrochim. Acta **2016**, *190*, 1050.

[22]   C. Song, D. Zhang, B. Wang, Z. Cai, P. Yan, Y. Sun, K. Ye, D. Cao, K. Cheng, G.
         Wang, *Nano Research* **2016**, *9*, 3322.

[23]   L. Yi, L. Liu, X. Liu, X. Wang, W. Yi, P. He, X. Wang, *Int. J. Hydrogen Energy* **2012**,
         37, 12650.
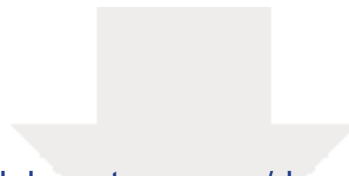
Click here to access/download
Supporting Information
Revised Supporting Information.doc
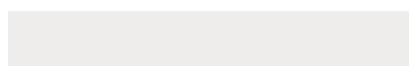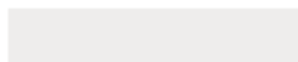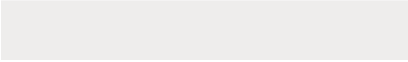
Click here to access/download
Production Data
Figure 1.tif
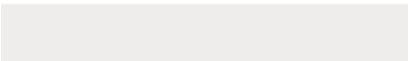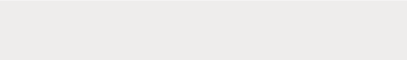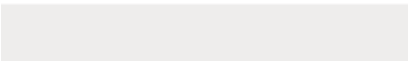
Click here to access/download
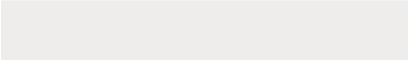**Production Data**
Figure 3.tif

Click here to access/download
Production Data
Figure 5.tif

Click here to access/download
Production Data
Figure 6.tif

Click here to access/download

Production Data

Scheme 1.tif

Click here to access/download
Production Data
the Table of contents.doc